Fragility of gate-error metrics in simulation models of flux-tunable transmon quantum computers

H. Lagemann,[1,2,*] D. Willsch,[1] M. Willsch,[1,3] F. Jin,[1] H. De Raedt,[1,4] and K. Michielsen[1,2,3]

[1]*Jülich Supercomputing Centre, Institute for Advanced Simulation, Forschungszentrum Jülich, 52425 Jülich, Germany*

[2]*RWTH Aachen University, 52056 Aachen, Germany*

[3]*AIDAS, Forschungszentrum Jülich, 52425 Jülich, Germany*

[4]*Zernike Institute for Advanced Materials, University of Groningen, Nijenborgh 4, 9747 AG Groningen, The Netherlands*

(Received 6 December 2022; accepted 19 July 2023; published 8 August 2023)

Constructing a quantum computer requires immensely precise control over a quantum system. A lack of precision is often quantified by gate-error metrics, such as the average infidelity or the diamond distance. However, usually such gate-error metrics are only considered for individual gates and not the errors that accumulate over consecutive gates. Furthermore, it is not well known how susceptible the metrics are to the assumptions which make up the model. Here we investigate these issues using realistic simulation models of quantum computers with flux-tunable transmons and coupling resonators. Our main findings reveal that (i) gate-error metrics are indeed affected by the many assumptions of the model, (ii) consecutive gate errors do not accumulate linearly, and (iii) gate-error metrics are poor predictors for the performance of consecutive gates. Additionally, we discuss a potential limitation in the scalability of the studied device architecture.

DOI: 10.1103/PhysRevA.108.022604

I. INTRODUCTION

The realization of a gate-based quantum computer in the real world is an engineering task which requires a tremendous amount of precision in terms of control over a quantum system. In this work we clearly differentiate between the following three concepts: The ideal gate-based quantum computer (IGQC), the prototype gate-based quantum computers (PGQCs), and the nonideal gate-based quantum computers (NIGQCs).

The state of an IGQC with $N \in \mathbb{N}$ qubits is described by a time-independent state vector $|\psi\rangle$ in a 2^N-dimensional Hilbert space as described in Refs. [1,2]. In this model changes of the state vector occur instantaneously by applying unitary operators $\hat{U}$ to the state vector $|\psi\rangle$. Therefore, all time-dependent aspects of gate errors which are omnipresent on PGQCs (see Refs. [3,4]) are neglected in this model. One often uses quantum operations (see Refs. [1,2]) to introduce gate errors to the IGQC model. Many gate-error metrics like the average gate infidelity (see Refs. [5,6]) and the diamond distance (see Refs. [7,8]) can be expressed in terms of quantum operations. However, also quantum operations do not describe the time-dependent aspects of gate errors.

In this work we are interested in modeling the appearance of gate errors as a real-time process. This type of modeling is motivated by the fact that superconducting PGQCs are physical systems and consequently one finds that these devices are inherently dynamic and affected by various internal and external factors. A review of the literature suggests that we have to take into account the variable control signals (see Refs. [9,10]), the temperature of the device (see Ref. [11]), temporal stability of device parameters such as the qubit frequency (see Ref. [12]), cosmic radiation (see Ref. [13]), and so on. Therefore, a complete mathematical description of these devices which takes into account all the relevant factors in one mathematical model seems prohibitive. However, we may be able to describe certain aspects of a superconducting PGQC by making use of simplified models. The simulations we perform to obtain the results presented in this work are intended to describe certain aspects of specific two-qubit, three-qubit, and four-qubit superconducting PGQCs. The device architecture, device parameters, and control pulses we use are similar to the ones used in experiments described in Refs. [14–16].

We define a NIGQC model as a model where the state of a gate-based quantum computer is described as a real-time entity. In this work the state of a NIGQC is by assumption completely determined by the state vector $|\Psi(t)\rangle$ and the dynamics of the system are generated by the time-dependent Schrödinger equation with $\hbar = 1$,

$$i\partial_t|\Psi(t)\rangle = \hat{H}(t)|\Psi(t)\rangle, \tag{1}$$

where $\hat{H}(t) = \hat{H}^\dagger(t)$ denotes a circuit Hamiltonian which is obtained by means of the lumped-element approximation (see Ref. [17]) and an associated effective Hamiltonian (see Ref. [18]). Note that the NIGQC models that we consider are idealized versions of the PGQCs used in experiments.

Our simulation software solves the time-dependent Schrödinger equation numerically with the product-formula algorithm (see Refs. [19,20]) for a given Hamiltonian $\hat{H}(t)$ and a sequence of control pulses which allows us to implement a sequence of gates with our NIGQC. This enables us to compute the gate errors for the individual gates in the program sequence. In the following, we call the sequence of gate errors which arises from this procedure a gate-error trajectory.

This paper is structured as follows. In Sec. II we specify the Hamiltonians $\hat{H}(t)$, the device parameters, and the control

*Corresponding author: hannes.a.l@me.com

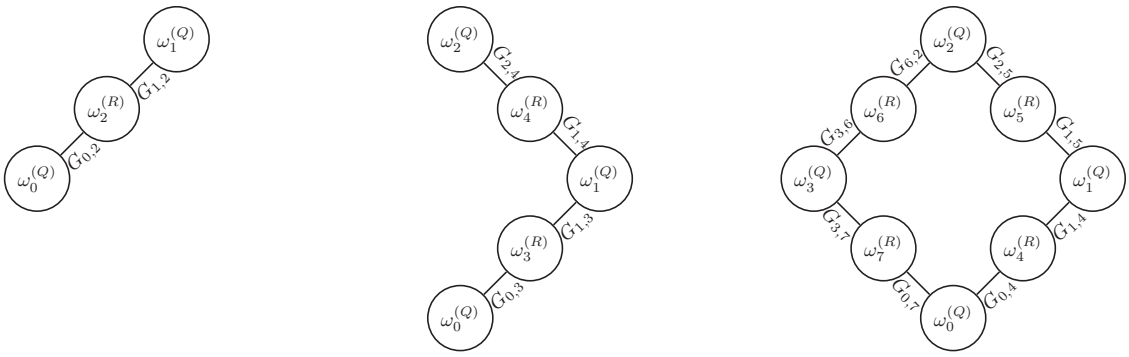

FIG. 1. Illustrations of flux-tunable transmon qubits with park qubit frequencies $\omega^{(Q)}$ and resonators with resonance frequencies $\omega^{(R)}$ which constitute NIGQCs with (a) $N = 2$, (b) $N = 3$, and (c) $N = 4$ qubits. The different subsystems are indexed with the discrete variable $i \in \{0, \ldots, 7\}$ such that the bare basis states of the system can be expressed as $|\mathbf{z}\rangle$, where $\mathbf{z} = (z_{|I|-1}, \ldots, z_0)$ is an n-tuple. The Hamiltonians we use to model the dynamics of our NIGQCs are given by Eqs. (2) and (7). The device parameters we use to specify the Hamiltonians are listed in Table I. The control pulses we use to implement the gates are displayed in Figs. 2(a)–2(c).

pulses we use to implement our NIGQC models. In Sec. III we discuss the gate-error metrics and how we compute them. In Sec. IV we present our findings. In Sec. IV A we discuss the spectrum of a four-qubit NIGQC and its relevance for the gate-error metrics we compute. In Sec. IV B we discuss the gate-error metrics we obtain by optimizing the parameters of the control pulses. In Sec. IV C we show how gate errors and the corresponding gate-error trajectories which arise over time are affected by modeling the dynamics of the system with different numbers of basis states. The gate errors in this section are obtained with the circuit Hamiltonian. In Sec. IV D we show how deviations in the control pulse parameters affect the gate-error trajectories. The gate errors in this section are also obtained with the circuit Hamiltonian. In Sec. IV E we show how the modeling of flux-tunable transmons as adiabatic and nonadiabatic anharmonic oscillators affects the gate errors over time. The gate errors in this section are obtained with an effective Hamiltonian. A summary, discussion, and the conclusions drawn are presented in Sec. V. Note that we use $\hbar = 1$ throughout this work.

To assist the reader in navigating through the material, we list the main findings.

(i) The authors of Ref. [3] concluded that the initial values for gate-error metrics like the diamond distance and the average infidelity are poor predictors of the future gate-error trajectories which emerge over time. In this work we provide new evidence which supports and strengthens this conclusion. Furthermore, we provide a concise theoretical explanation for why this is the case and how we should interpret gate-error metrics like the diamond distance and the average infidelity (see Secs. IV C–IV E).

(ii) By analyzing the spectrum of a four-qubit NIGQC, we discuss a problem which potentially limits the upscaling capabilities of device architectures which implement two-qubit gates by tuning the energies of basis states into resonance with one another. The issues we discuss implicate an exponentially large optimization problem for future quantum computer engineers (see Sec. IV A).

(iii) By simulating the time evolution of different NIGQC models, we explicitly show that even seemingly small changes in the assumptions which make up the underlying model can substantially affect the gate-error metrics. The fact itself is not surprising. However, the extent to which the changes affect the gate-error metrics during the course of the time evolution of the system is something worth knowing (see Secs. IV C–IV E).

(iv) By executing simple gate repetition programs on different NIGQCs, we show that gate-error metrics in NIGQC models do not behave linearly. Furthermore, we also show that gate-error metrics respond to changes in the model in a nonlinear manner (see Sec. IV C–IV E). Given these findings, we conjecture that gate errors for consecutive gates are not simply given by the sum of the gate errors for the individual gates in the program sequence but emerge due to a complex interplay of small deviations with respect to the target gates which occur over time.

II. MODELS AND DEVICE PARAMETERS

Figures 1(a)–1(c) show illustrations of the two-qubit, three-qubit, and four-qubit NIGQCs we consider in this work, respectively. The parameters $\omega^{(Q)}$ denote the park qubit frequencies for the different flux-tunable transmon qubits. The park qubit frequency is the frequency at which a transmon qubit resides if no external flux is applied. Similarly, the parameters $\omega^{(R)}$ refer to LC resonator frequencies. In the following, we will simply call these systems transmon qubits and resonators. The interactions between the different transmon qubits are conveyed by the resonators. We model the interactions between the different subsystems as dipole-dipole interactions and use the constants $G_{i,j}$, where $i, j \in \mathbb{N}^0$, to control the interaction strength. The device parameters listed in Table I are used for all simulations in this work.

The remainder of this section is devoted to the models we use to describe the dynamics of the NIGQCs in Figs. 1(a)–1(c). In Sec. II A we introduce a circuit Hamiltonian. In Sec. II B we introduce an effective Hamiltonian which is related to the circuit Hamiltonian. Finally, in Sec. II C we define the control pulses we use to implement the different gates.

TABLE I. Device parameters for a four-qubit virtual chip. The device architecture and device parameters are motivated by experiments described in Refs. [14–16]. The index i denotes the different circuit elements which are part of the system (in total there are eight circuit elements). The parameter $\omega_i^{(R)}$ denotes the coupler frequency, i.e., the transmission line resonator frequency. Since all couplers have the same frequency, we show only one row for all coupling resonators; see the last row where $i \in \{4, 5, 6, 7\}$. The constants $\omega_i^{(Q)}$ and $\alpha_i^{(Q)}$ denote the qubit frequency and anharmonicity, respectively. The parameter E_{C_i} denotes the capacitive energy of the ith qubit. Similarly, $E_{J_i,r}$ and $E_{J_i,l}$ denote the corresponding Josephson energies. Note that in this work we express the Hamiltonian in Eq. (4) with a factor of E_C instead of $4E_C$. This means we adopt the original convention used in Ref. [21] and not the one of Ref. [22]. The parameter $\varphi_{0,i}$ denotes the so-called flux offset, i.e., the external flux $\varphi_{0,i}(t)$ at time $t = 0$. The interaction strength $G_{i,j}$ between the different circuit elements is set to 300 MHz for all $i, j \in \mathbb{N}^0$. All units (except the one of the flux offset) are in gigahertz. The flux offset is given in units of the flux quantum Φ_0. We use these device parameters to model the two-qubit, three-qubit, and four-qubit NIGQCs illustrated in Figs. 1(a)–1(d). Note that we use $\hbar = 1$ throughout this work.

i	$\omega_i^{(R)}/2\pi$	$\omega_i^{(Q)}/2\pi$	$\alpha_i^{(Q)}/2\pi$	$E_{C_i}/2\pi$	$E_{J_i,l}/2\pi$	$E_{J_i,r}/2\pi$	$\varphi_{0,i}/2\pi$
0	n/a	4.200	−0.320	1.068	2.355	7.064	0
1	n/a	5.200	−0.295	1.037	3.612	10.837	0
2	n/a	5.700	−0.285	1.017	4.374	13.122	0
3	n/a	4.960	−0.300	1.045	3.281	9.843	0
4–7	45.000	n/a	n/a	n/a	n/a	n/a	n/a

The device architecture, device parameters, and control pulses we use are motivated by experiments described in Refs. [14–16].

A. Circuit Hamiltonian model

The circuit Hamiltonian we use to model our NIGQCs is defined as

$$\hat{H}_{\text{cir}} = \hat{H}_{\text{res},\Sigma} + \hat{H}_{\text{tun},\Sigma} + \hat{V}_{\text{int}}. \tag{2}$$

The first term

$$\hat{H}_{\text{res},\Sigma} = \sum_{k\in K} \omega_k^{(R)} \hat{a}_k^\dagger \hat{a}_k \tag{3}$$

describes a collection of noninteracting resonators. Here $K \subseteq \mathbb{N}^0$ denotes an index set for the resonators and $\omega_k^{(R)}$ refers to the different resonator frequencies. The operators $\hat{a}$ and $\hat{a}^\dagger$ are the bosonic annihilation and creation operators, respectively.

Similarly, the second term

$$\begin{aligned}\hat{H}_{\text{tun},\Sigma} = \sum_{j\in J} \Big\{ & E_{C_j}[\hat{n}_j - n_j(t)]^2 + \left(\frac{1}{2} - \beta_j\right)\dot{\varphi}_j(t)\hat{n}_j \\ & - E_{J_{l,j}} \cos[\hat{\varphi}_j + \beta_j \varphi_j(t)] \\ & - E_{J_{r,j}} \cos[\hat{\varphi}_j + (\beta_j - 1)\varphi_j(t)] \Big\}\end{aligned} \tag{4}$$

describes a collection of noninteracting flux-tunable transmons. Here $J \subseteq \mathbb{N}^0$ denotes an index set for the transmon qubits. Furthermore, the parameters E_{C_j}, $E_{J_{l,j}}$, and $E_{J_{r,j}}$ denote the capacitive energies, the left Josephson energies, and the right Josephson energies, respectively. Note that the Hamiltonian in Eq. (4) is often expressed with a factor $4E_C$ instead of E_C. In this work we adopt the original convention used in Ref. [21] and not the one of Ref. [22]. The parameters β_j are not device parameters but determine the variables we use for the quantization of the circuit. We use $\beta_j = \frac{1}{2}$ for all simulations in this work (cf. Refs. [23,24]). In Appendix A we provide a detailed derivation of the Hamiltonian for a single flux-tunable transmon with a charge drive term. This derivation is motivated by the work in Ref. [23].

The device parameters in Table I were obtained as follows. The Quantum Device Lab, which is affiliated with the ETH Zurich, provided us with the qubit frequencies $\omega_j^{(Q)}$, anharmonicities $\alpha_j^{(Q)}$, and asymmetry factors d_j for the various transmon qubits in the system as well as the coupling resonator frequencies $\omega_k^{(R)} = 45$ GHz. We then used the relations

$$\omega_j^{(Q)} = \left(E_j^{(1)} - E_j^{(0)}\right), \tag{5a}$$

$$\alpha_j^{(Q)} = \left(E_j^{(2)} - E_j^{(0)}\right) - 2\omega_j^{(Q)}, \tag{5b}$$

$$d_j = \frac{E_{J_{r,j}} - E_{J_{l,j}}}{E_{J_{r,j}} + E_{J_{l,j}}} \tag{5c}$$

and the Hamiltonian (4) to fit the energy levels $E_j^{(0)}$, $E_j^{(1)}$, and $E_j^{(2)}$ to the provided data.

The third term

$$\hat{V}_{\text{int}} = \sum_{(k,j)\in K\times J} G_{k,j}(\hat{a}_k + \hat{a}_k^\dagger) \otimes \hat{n}_j \tag{6}$$

describes dipole-dipole interactions between resonators and transmon qubits. Here $G_{k,j}$ is a real-valued constant which is set to 300 MHz for all simulations in this work. This value for interaction strength constants $G_{k,j}$ roughly reproduces the gate durations of around 100 ns which were found to be appropriate in the experiment.

For our simulations of the Hamiltonian (2) we use the product-formula algorithm (see Refs. [19,20]) and what we call a bare basis. This bare basis is formed by the tensor product states of the harmonic oscillator and the transmon basis states, which are obtained for the external flux $\varphi_j(t)$ at time $t = 0$. In this paper we model the dynamics of the Hamiltonian (2) with four basis states for all resonators and most transmon qubits are modeled with 16 basis states. Only the transmon qubit with the index $i = 0$ [see Figs. 1(a)–1(c)] is modeled with four basis states. Note that this transmon does not experience a flux drive. Therefore, we can model this transmon with four basis states only. There is one exception to this rule, namely, the results in Sec. IV C are obtained with four and 16 basis states for all transmon qubits.

B. Effective Hamiltonian model

The approximations which are needed to obtain the effective Hamiltonian defined in this section are discussed in detail in Ref. [18]. Furthermore, the full effective model is defined in terms of 12 equations. In order to provide a concise discussion of the effective model, we only discuss the most relevant relations. A more detailed discussion of the effective model with all 12 equations can be found in Appendix B.

The effective Hamiltonian we use to model our NIGQCs is defined by

$$\hat{H}_{\text{eff}} = \hat{H}_{\text{res},\Sigma} + \hat{H}_{\text{tun eff},\Sigma} + \hat{D}_{\text{charge},\Sigma} + \hat{\mathcal{D}}_{\text{flux},\Sigma} + \hat{W}_{\text{int}}. \quad (7)$$

The second term

$$\hat{H}_{\text{tun eff},\Sigma} = \sum_{j\in J} \omega_j^{(q)}(t)\hat{b}_j^\dagger \hat{b}_j + \frac{\alpha_j^{(q)}(t)}{2}[\hat{b}_j^\dagger \hat{b}_j(\hat{b}_j^\dagger \hat{b}_j - \hat{I})] \quad (8)$$

describes a collection of noninteracting flux-tunable transmons which are modeled as adiabatic, anharmonic oscillators in a time-dependent basis. The operators $\hat{b}$ and $\hat{b}^\dagger$ are the bosonic annihilation and creation operators, respectively. The functions $\omega_j^{(q)}(t)$ and $\alpha_j^{(q)}(t)$ [see Eqs. (B4) and (B7)] denote the flux-tunable qubit frequency and anharmonicity, respectively. Note that the time dependence in both these functions is given by the external flux $\varphi_j(t)$. In this work we use the series expansions obtained by the authors of Ref. [25] to approximate the three lowest energy levels of Hamiltonian (4) for the external flux values $\varphi_j(t)$ at any given point in time.

The third term

$$\hat{D}_{\text{charge},\Sigma} = \sum_{j\in J} \Omega_j(t)(\hat{b}_j^\dagger + \hat{b}_j) \quad (9)$$

describes a charge drive. Here $\Omega_j(t) \propto -2E_{C_j} n_j(t)$ and we approximate the charge operators $\hat{n}_j$ by effective charge operators $\hat{n}_{j,\text{eff}}$, which can be expressed in terms of the bosonic operators (see Ref. [22]).

The fourth term

$$\hat{\mathcal{D}}_{\text{flux},\Sigma} = \sum_{j\in J}\Bigg(-i\sqrt{\frac{\xi_j(t)}{2}}\dot{\varphi}_{\text{eff},j}(t)(\hat{b}_j^\dagger - \hat{b}_j) + \frac{i}{4}\frac{\dot{\xi}_j(t)}{\xi_j(t)}(\hat{b}_j^\dagger \hat{b}_j^\dagger - \hat{b}_j\hat{b}_j)\Bigg) \quad (10)$$

describes a nonadiabatic flux drive. Here $\dot{\varphi}_{\text{eff},j}(t) \propto \dot{\varphi}_j(t)$ and $\dot{\xi}_j(t)/\xi_j(t) \propto \dot{\varphi}_j(t)$. Note that $\dot{\varphi}_{\text{eff},j}(t)$ and $\xi_j(t)$ are given by Eqs. (B10a) and (B10c). This term results from the fact that we model the effective flux-tunable transmon in a time-dependent basis. Consequently, for the time-dependent Schrödinger equation to stay form invariant (see Ref. [18]), a time-dependent basis transformation term is needed.

The fifth term

$$\hat{W}_{\text{int}} = \sum_{(k,j)\in K\times J} g_{k,j}^{(a,b)}(t)(\hat{a}_k^\dagger + \hat{a}_k)\otimes(\hat{b}_j^\dagger + \hat{b}_j) \quad (11)$$

describes time-dependent dipole-dipole interactions. The time dependence of the interaction strength is a result of the fact that we model the effective flux-tunable transmon in a time-dependent basis (see Ref. [18]). The function $g_{k,j}^{(a,b)}(t)$ is given by Eq. (B16). This time-dependent interaction strength model is motivated by the work in Ref. [22].

As before, we use the product-formula algorithm (see Refs. [19,20]) to solve the time-dependent Schrödinger equation for the Hamiltonian (7). Here we use a bare basis that is formed by the tensor product states of the time-independent (for the resonators) and time-dependent (for the transmon qubits) harmonic oscillator for the simulations. The dynamics of Hamiltonian (7) is modeled with four basis states for all resonators and transmons.

C. Control pulses and gate implementations

Figures 2(a)–2(c) show the external charge $n(t)$ [Fig. 2(a)] and the external flux $\varphi(t)$ [Figs. 2(b) and 2(c)] as functions of time t. In Fig. 2(a) we show a microwave pulse (MP), in Fig. 2(b) we show a unimodal pulse (UMP), and in Fig. 2(c) we show a bimodal pulse (BMP). In this section we introduce the functions which are used to obtain the data we show in Figs. 2(a)–2(c). We use these functions as control pulses for our NIGQC models.

For the single-qubit gates we use the external charge

$$n(t) = aG(t,\sigma,T_d)\cos(\omega^{(D)}t - \phi) + b\dot{G}(t,\sigma,T_d)\sin(\omega^{(D)}t - \phi) \quad (12)$$

to drive transitions that can be used to implement $R^{(x)}(\pi/2)$ rotations with a microwave control pulse. Here $G(t,\sigma,T_d)$ is a Gaussian envelope function centered around half of the pulse duration T_d. The width and the shape of the Gaussian are determined by the parameters σ and T_d. Furthermore, a denotes the pulse amplitude, $\omega^{(D)}$ refers to the drive frequency, b is the amplitude of the derivative removal by adiabatic gate (DRAG) pulse component (see Ref. [26]), and ϕ is the phase of the pulse. We use the phase ϕ in Eq. (12) to implement virtual Z gates (see Ref. [27]) on our NIGQCs.

Two-qubit controlled-Z (CZ) gates can be implemented with an external flux of the form

$$\varphi(t) = \frac{\delta}{2}\left[\text{erf}\left(\frac{t}{\sqrt{2}\sigma}\right) - \text{erf}\left(\frac{t-T_p}{\sqrt{2}\sigma}\right)\right], \quad (13)$$

where δ denotes the pulse amplitude, σ is a parameter which allows us to control how fast the pulse flanks rise and fall, T_p is the pulse time, and erf denotes the Gauss error function. Note that in the computer program we add an additional free time evolution (the buffer time) to the pulse such that the complete pulse duration T_d is longer than T_p. We refer to this pulse as the UMP.

We can also use the external flux

$$\varphi(t) = \frac{\delta}{2}\left[\text{erf}\left(\frac{t}{\sqrt{2}\sigma}\right) - 2\,\text{erf}\left(\frac{t-T_p/2}{\sqrt{2}\sigma}\right) + \text{erf}\left(\frac{t-T_p}{\sqrt{2}\sigma}\right)\right] \quad (14)$$

to implement two-qubit CZ gates. This pulse is referred to as the BMP. Note that the BMP pulse is sometimes referred to as net-zero flux pulse. The UMP and the BMP are also used to implement gates in experiments (see Refs. [9,14–16]).

Every CZ gate in our NIGQC model is implemented by means of a flux pulse $\varphi(t)$ followed by single-qubit z-axis rotations $R_i^{(z)}(\phi_i)$ for every qubit in the NIGQC model (see Ref. [28]). Since the z-axis rotation parameters ϕ_i are quite numerous, e.g., a four-qubit system with four CZ gates has 16

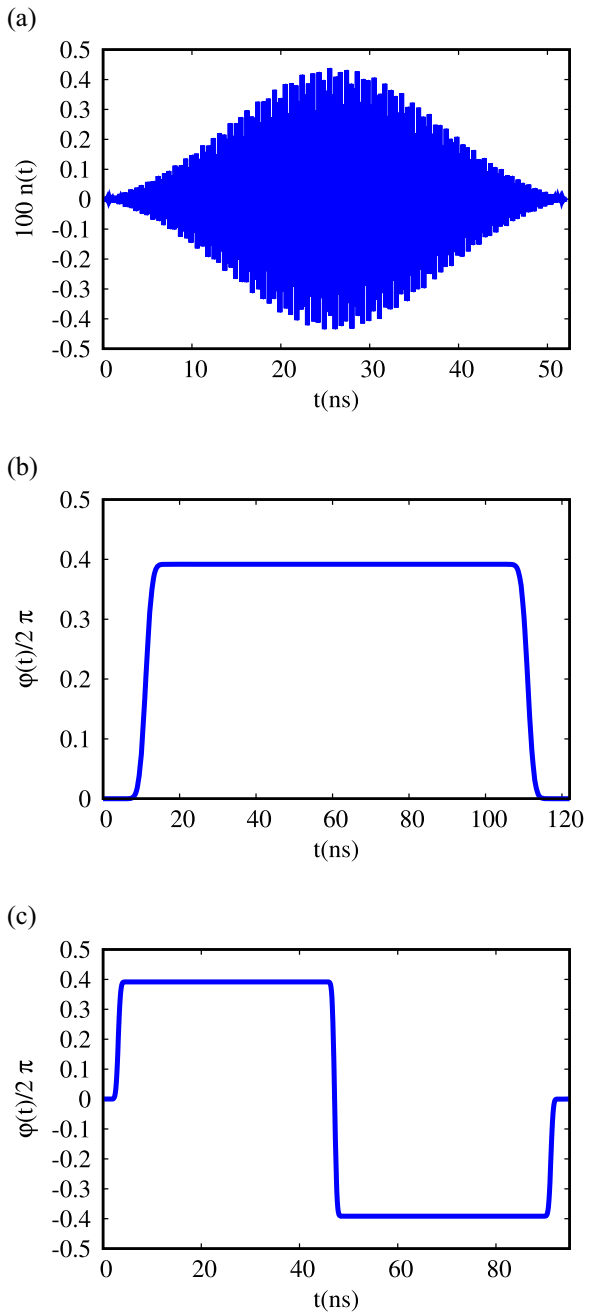

FIG. 2. (a) External charge $n(t)$ given by Eq. (12) and external fluxes $\varphi(t)$ given by (b) Eq. (13) and (c) Eq. (14) as a functions of time t for the (a) microwave pulse, (b) unimodal pulse, and (c) bimodal pulse. In the circuit model both functions $n(t)$ and $\varphi(t)$ enter via the Hamiltonian (4). In the effective model both functions $n(t)$ and $\varphi(t)$ enter via the driving terms (9) and (10), respectively. Moreover, in the effective model the external flux $\varphi(t)$ also enters the time-dependent interaction strength in Eq. (11) and the tunable qubit frequency and anharmonicity in Eq. (8) (see Appendix B for more details).

of these parameters, we omit the ϕ_i phases from the control pulse parameter (Tables IX–XIX in Appendix D). Finally, we execute these z-axis rotations by means of virtual Z gates in combination with a transformation of the frame of reference, which affects only the phases of the state vector but not the state vector amplitudes (see Sec. 3.3.2 in Ref. [29]).

III. COMPUTATION OF GATE-ERROR QUANTIFIERS

In this section we discuss the gate-error quantifiers we compute as well as how we determine the numerical values.

A computation in the IGQC model can be understood as a mapping

$$|\psi\rangle \mapsto |\psi'\rangle \tag{15}$$

between an initial state $|\psi\rangle$ and a final state $|\psi'\rangle$ and the state vector of an N-qubit IGQC can be expressed as

$$|\psi\rangle = \sum_{\mathbf{z}\in\{0,1\}^N} c_{\mathbf{z}}|\mathbf{z}\rangle, \tag{16}$$

where $\{|\mathbf{z}\rangle\}$ are the 2^N computational basis states of the IGQC. All state vectors $|\psi\rangle$ are normalized complex vectors in a finite-dimensional Hilbert space $\mathcal{H}^{2^N}$. The computation is described by a unitary operator $\hat{U}$.

One simple error measure is the statistical distance

$$\mu_{\mathrm{SD}}(\mathbf{p},\tilde{\mathbf{p}}) = \frac{1}{2}\sum_{\mathbf{z}\in\{0,1\}^N} \|p_{\mathbf{z}} - \tilde{p}_{\mathbf{z}}\|_1, \tag{17}$$

where by definition $p_{\mathbf{z}} = \|\langle\mathbf{z}|\psi\rangle\|_1^2$ are the probability amplitudes of the IGQC (which we use as a reference distribution to compare against) and $\tilde{p}_{\mathbf{z}}$ denotes the actual distribution that is being evaluated. This distribution can be generated by either a PGQC or a NIGQC. Furthermore, $\|\cdot\|_1$ denotes the absolute value. The advantage of the statistical distance is that we can more or less easily measure the relative frequencies $p_{\mathbf{z}}$ in an experiment. While such an error measure is useful in practice (see Refs. [3,4,29]) it neglects the phase information of the state vector $|\psi\rangle$. Moreover, the statistical distance only provides a measure of closeness for one particular input state. For this reason, usually more sophisticated gate-error metrics are considered.

Most gate metrics are defined in terms of quantum operations. From a mathematical point of view, quantum operations are superoperators $\check{\mathcal{E}}(\hat{\rho})$ which act on the space of density operators $\hat{\rho}\in\mathcal{P}$. Additionally, we require $\check{\mathcal{E}}$ to be linear, Hermiticity preserving, and completely positive (see Refs. [1,2]). Note that if one can also show that $\check{\mathcal{E}}$ is trace preserving, $\check{\mathcal{E}}$ is usually referred to as a quantum or error channel.

The error metrics we consider in this work can be expressed in terms of the two quantum operations

$$\check{\mathcal{E}}_{\mathrm{U}}(\hat{\rho}) = \hat{U}\hat{\rho}\hat{U}^{\dagger} \tag{18}$$

and

$$\check{\mathcal{E}}_{\mathrm{M}}(\hat{\rho}) = \hat{M}\hat{\rho}\hat{M}^{\dagger}, \tag{19}$$

where $\hat{\rho} = |\psi\rangle\langle\psi|$ and $|\psi\rangle\in\mathcal{H}^{2^N}$. The operator $\hat{M}$ in Eq. (19) is defined as

$$\hat{M} = \hat{P}\hat{\mathcal{U}}(t,t_0)\hat{P}, \tag{20}$$

where $\hat{P}$ is a projection operator onto the computational space and $\hat{\mathcal{U}}$ denotes the formal solution of the time-dependent Schrödinger equation

$$\hat{\mathcal{U}}(t,t_0) = \mathcal{T}\exp\left(-i\int_{t_0}^{t}\hat{H}(t')dt'\right). \tag{21}$$

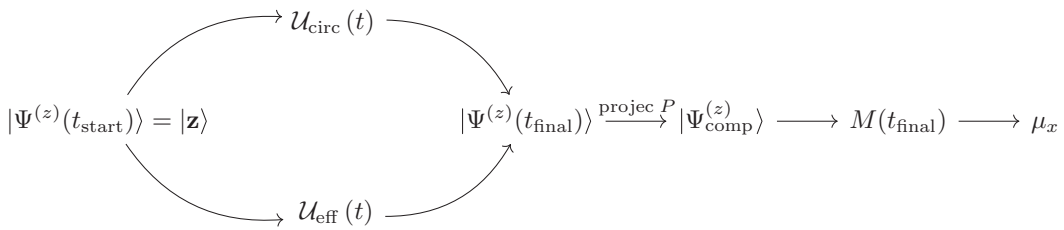

FIG. 3. Illustration of the computational process we use to obtain the gate-error quantifiers μ_x. Here x is a label for an arbitrary metric and $\hat{\mathcal{U}}_{\rm cir}$ ($\hat{\mathcal{U}}_{\rm eff}$) is the time-evolution operator in Eq. (21) for the circuit (effective) Hamiltonian given by Eq. (2) [Eq. (7)]. We compute the state vectors $|\Psi^{(z)}(t_{\rm final})\rangle$ with a product-formula algorithm (see Refs. [19,20]) for all computational basis states 2^N of a NIGQC and then store the data in the matrix $M(t_{\rm final})$. In this matrix, every column corresponds to the evolution of one computational state $|\Psi^{(z)}_{\rm comp}\rangle = P|\Psi^{(z)}(t_{\rm final})\rangle$, where P denotes a projection matrix onto the computational subspace. We use the message passing interface to parallelize the 2^N independent tasks. The computations are performed on the supercomputer JUWELS (see Ref. [31]). Finally, we compute the metric μ_x with regard to a target operation U. The metrics we compute provide a measure for how close M and U are.

Here $\mathcal{T}$ is the time-ordering symbol. In addition, the Hamiltonian $\hat{H}$ is given by either Eq. (2) or (7).

The first error metric that we consider is the average fidelity

$$\mu_{\rm F_{avg}} = \int \langle\psi|\check{\mathcal{E}}_{\rm M}\check{\mathcal{E}}_{\rm U}^{-1}(|\psi\rangle\langle\psi|)|\psi\rangle d|\psi\rangle, \tag{22}$$

where the integral is taken over all states $|\psi\rangle \in \mathcal{H}^{2^N}$ in the Hilbert space. If we define the auxiliary operator

$$\hat{V} = \hat{U}\hat{M}^\dagger, \tag{23}$$

we can express the average fidelity as

$$\mu_{\rm F_{avg}} = \frac{\|{\rm Tr}(\hat{V})\|_1^2 + {\rm Tr}(\hat{M}\hat{M}^\dagger)}{D(D+1)}, \tag{24}$$

where $D = 2^N$. This is expression is derived in Sec. 7 in Ref. [6]. We can use the average fidelity to define the average infidelity

$$\mu_{\rm IF_{avg}} = 1 - \mu_{\rm F_{avg}}. \tag{25}$$

In order to define a leakage measure for our NIGQCs, we make use of the second term in the numerator of Eq. (24). We define the leakage measure as

$$\mu_{\rm leak} = 1 - \left(\frac{{\rm Tr}(\hat{M}\hat{M}^\dagger)}{D}\right), \tag{26}$$

where ${\rm Tr}(\hat{M}\hat{M}^\dagger)$ can be expressed as the sum of probability amplitudes. Hence, we find $0 \leqslant {\rm Tr}(\hat{M}\hat{M}^\dagger) \leqslant D$, and therefore it follows that $\mu_{\rm leak} \in [0, 1]$.

The second error metric we consider is the diamond distance

$$\mu_\diamond = \tfrac{1}{2}\left\|\check{\mathcal{E}}_{\rm M}\check{\mathcal{E}}_{\rm U}^{-1} - \hat{I}\right\|_\diamond, \tag{27}$$

where $\|\cdot\|_\diamond$ denotes the diamond norm (see Refs. [7,8]). We can express the diamond distance in terms of an infimum

$$\mu_\diamond = \tfrac{1}{2}\inf_{Q\in{\rm GL}_4(\mathbb{C})}\left\{\|(\hat{V},\hat{I})\hat{Q}^{-\dagger}\hat{Q}^{-1}(\hat{V},\hat{I})^T\|_2^{1/2} \times \|(\hat{V},-\hat{I})\hat{Q}^{\dagger}\hat{Q}^{1}(\hat{V},-\hat{I})^T\|_2^{1/2}\right\} \tag{28}$$

over all complex, invertible, 2×2 matrices (see Ref. [30]). Similarly, we can express the diamond distance in terms of a supremum

$$\mu_\diamond = \tfrac{1}{2}\sup_{|\psi\rangle\in\mathcal{H}^{2^N}}\{\|(\hat{V}^\dagger\otimes\hat{I})|\psi\rangle\langle\psi|(\hat{V}^\dagger\otimes\hat{I})^\dagger - |\psi\rangle\langle\psi|\|_{\rm Tr}\}, \tag{29}$$

over all state vectors of the Hilbert space of the IGQC (see Ref. [2]). We obtain the diamond distance up to the fourth decimal by cornering

$$\mu_\diamond^{(\rm inf)} \leqslant \mu_\diamond \leqslant \mu_\diamond^{(\rm sup)}, \tag{30}$$

with the value $\mu_\diamond$ with the infimum $\mu_\diamond^{(\rm inf)}$ and supremum $\mu_\diamond^{(\rm sup)}$ expressions in Eqs. (28) and (29). The algorithms we use are discussed in Sec. 6.1.2 in Ref. [29].

Figure 3 illustrates the computational process we use to obtain the matrix M and in turn the various gate-error quantifiers μ_x in this work. The label x denotes an arbitrary metric or measure. First, we simulate the time evolution $|\Psi^{(z)}(t_{\rm final})\rangle$ of the system for all 2^N basis states $|\Psi^{(z)}(t_{\rm start})\rangle = |\mathbf{z}\rangle$ of the NIGQC. Note that we simulate the 2^N time evolutions $|\Psi^{(z)}(t)\rangle$ in parallel on the supercomputer JUWELS (see Ref. [31]). Then we make use of a projection matrix P and map the state vectors to the computational states $|\Psi^{(z)}_{\rm comp}\rangle = P|\Psi^{(z)}(t_{\rm final})\rangle$. Finally, we store the data by building the matrix

$$M = \sum_{\mathbf{z}\in\{0,1\}^N} |\Psi^{(z)}_{\rm comp}\rangle\langle\mathbf{z}|, \tag{31}$$

where $|\mathbf{z}\rangle$ are the Cartesian unit vectors, in the computer program. Finally, we compute the gate-error quantifiers μ_x by means of the matrix $V = UM^\dagger$.

IV. RESULTS

In this section we present our findings. First, in Sec. IV A we discuss the spectrum of the four-qubit NIGQC illustrated in Fig. 1(c) and its relevance for the gate-error metrics we compute. Here we model the system with the circuit Hamiltonian (2). Next, in Sec. IV B we discuss the results of the calibration process for the different NIGQCs illustrated in Figs. 1(a)–1(c). Here we consider both the circuit and the effective model. Then, in Sec. IV C we show how modeling the time evolution of NIGQCs with more and less basis states affects the gate-error quantifiers. Here we use the

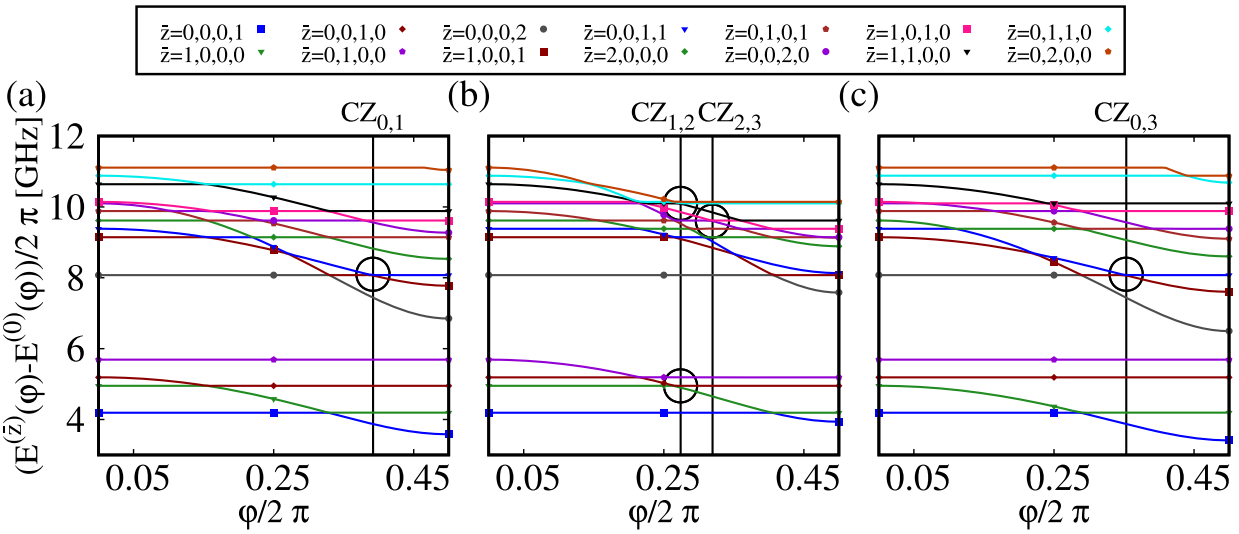

FIG. 4. Lowest 14 energy levels of the four-qubit NIGQC illustrated in Fig. 1(c) as functions of the external flux offset φ for (a) the second ($i = 1$), (b) the third ($i = 2$), and (c) the fourth ($i = 3$) transmon qubit. We use the circuit Hamiltonian (2) and the device parameters listed in Table I to obtain the results with a standard diagonalization algorithm (see Ref. [39]). All transmons are modeled with three basis states and all resonators are modeled with two basis states. We also mark (vertical lines) the pulse amplitudes δ used to implement the CZ gates on the four-qubit NIGQC. Furthermore, we mark important energy level repulsions (ELRs) by means of black circles. In (b) we can observe that the pulse amplitude for the $\mathrm{CZ}_{1,2}$ gate is near two ELRs. The first one is in the energy band between 4 and 6 GHz. This ELR leads to unwanted transitions between the first excited states of two qubits. The second one is in the energy band between 9 and 11 GHz. This ELR is used to implement the $\mathrm{CZ}_{1,2}$ gate. In (a)–(c) we can observe that the other CZ gates do not suffer from the same problem. Moreover, we can observe that driving different transmons (a) $i = 1$, (b) $i = 2$, and (c) $i = 3$ leads to different spectral patterns.

circuit Hamiltonian (2) to model the dynamics of the four-qubit NIGQC illustrated in Fig. 1(c). In Sec. IV D we show how small deviations in a single control pulse parameter can affect gate-error metrics. Here we use the circuit Hamiltonian (2) to model the dynamics of the two-qubit, three-qubit, and four-qubit NIGQCs illustrated in Figs. 1(a)–1(c), respectively. Finally, in Sec. IV E we show how the commonly used adiabatic approximation for flux-tunable transmons affects gate-error metrics. Here we use the adiabatic and nonadiabatic effective Hamiltonian (2) to model the dynamics of the two-qubit, three-qubit, and four-qubit NIGQCs illustrated in Figs. 1(a)–1(c).

A. Spectrum for a four-qubit NIGQC

In this section we discuss the spectrum of the four-qubit NIGQC illustrated in Fig. 1(c) and its relevance for the implementation of two-qubit gates.

Broadly speaking, the general idea of implementing two-qubit CZ gates with a UMP or BMP is to tune a target computational state like $|0, 0, 1, 1\rangle$ into resonance with a noncomputational state like $|0, 0, 0, 2\rangle$, wait some time until the population returns to the computational target state, and hope that this state has gained an additional phase of $e^{i\pi}$ with respect to all the other computational states of the NIGQC. The word "tune" in this context refers to tuning the energies of the instantaneous eigenstates of the system, i.e., the discussion is implicitly carried out in the instantaneous basis of the system. Additionally, single-qubit z-axis rotations $R_i^{(z)}(\phi_i)$ are used to improve the performance (see Ref. [28]).

The time it takes for our devices to swap the population back and forth between a computational and a noncomputational state of the NIGQC lies between 75 and 100 ns. This time corresponds to the plateau time in Figs. 2(b) and 2(c). We fix these times by choosing the interaction strength constant G such that we approximately obtain the same gate times as in the experiment. Furthermore, the pulse amplitude δ or the plateau height is fixed by the condition that the states involved in this process should have close-by energies. The time it takes to reach the plateau is crucial; we discuss this part of the gate implementation later in this section.

In Ref. [28] the authors differentiated between gates that are implemented adiabatically (see Ref. [32]) and gates that are implemented nonadiabatically (see Ref. [33]). However, in the context of quantum theory the words adiabatic and nonadiabatic are usually associated with the adiabatic approximation (see Sec. 6.6 in Ref. [34]). Note that the process described above is clearly not an adiabatic one, i.e., the probability amplitudes of the state vector change over time. This and the fact that in almost all studies the transmon qubit is modeled as an adiabatic anharmonic oscillator or as an adiabatic two-level system lead us to the conclusion that in the context of the gate implementation protocol described above the words adiabatic and nonadiabatic are simply used to differentiate between gates with short and long pulse durations. Note that in Sec. IV E we investigate a related issue. There are two additional problems with the picture described above. First, assigning labels to the energies $E_z(\varphi)$ and eigenstates $|\phi_z(\varphi)\rangle$ of a continuous set of Hermitian matrices $\{H(\varphi)\}$, where $z \in \mathbb{N}^0$ and $\varphi/2\pi \in [0, 1]$, is a nontrivial problem in itself (see Refs. [35–38]). Second, once we apply a UMP or BMP flux drive, we cannot guarantee that only the desired transitions occur. In order to provide clarity on these issues, in the discussion of the four-qubit NIGQC spectrum, we do not adopt the same nomenclature used in Ref. [28].

Figures 4(a)–4(c) show the 14 lowest energy levels of the four-qubit NIGQC illustrated in Fig. 1(c) as functions of the external flux offset φ for the second ($i = 1$) transmon qubit [Fig. 4(a)], the third ($i = 2$) transmon qubit [Fig. 4(b)], and the fourth ($i = 3$) transmon qubit [Fig. 4(c)]. This means that each panel is obtained by repeatedly diagonalizing the matrix for different flux offset values $\varphi/2\pi \in [0, 0.5]$. The results are obtained with the circuit Hamiltonian (2), the device parameters listed in Table I, and a standard diagonalization algorithm (see Ref. [39]). Here we use two basis states for the coupling resonators and three basis states for the different transmon qubits in the system. Note that the circuit Hamiltonian (4) has two symmetry points, one at $\varphi/2\pi = 0.5$ and one at $\varphi/2\pi = 1$.

We label the energies $E_{\tilde{z}}$ of the interacting system according to the sorted energies E_z of the noninteracting system for the flux offset $\varphi = 0$. The markers in Figs. 4(a)–4(c) are there to guide the eye. Additionally, we employ black vertical lines to mark the flux offset values φ that correspond to pulse amplitudes δ for the CZ gates in Table XIII. Furthermore, we employ black circles to mark the energy level repulsions (ELRs) that we use to implement the CZ gates and the ELRs that are problematic for the implementation of CZ gates with low gate-error metrics [see the line with two circles in Fig. 4(b)].

If we start at the flux offset value $\varphi = 0$ and then move to a value $\varphi = \delta$ by driving a transmon qubit, we usually pass through several unused ELRs, i.e., not used to implement the CZ gates, with some of the computational basis states of the NIGQC before we reach the ELR or the flux offset value that we use to implement the CZ gate. Here we have to pass through the unused ELRs sufficiently fast because otherwise we can observe population exchange between the two states involved. This can be clearly observed (data not shown) if one studies the matrix in Eq. (31) while optimizing the control pulse parameters or the probability amplitudes themselves during the time evolution of the system. Also, one cannot move the system too fast; otherwise one observes (data not shown) all sorts of other transitions, e.g., the excited coupler states suddenly become populated. The pulse optimization algorithm that we employ finds a balance between these two mechanisms and fine-tunes the pulse amplitude δ and the remaining pulse parameters such that nearly perfect population exchange occurs and the phases are aligned properly. Note that we have to take all 2^N computational basis states into account (see Fig. 3).

In Fig. 4(b) we can also identify a problem that the optimization cannot solve on its own (see the line with two circles). The ELR in the energy band between 4 and 6 GHz induces a population exchange between two computational states of the NIGQC and is therefore unwanted. In addition, in the energy band between 9 and 12 GHz for the same flux offset value, we can observe a dense structure of energy levels with many nearby ELRs.

Obviously, this leads to the question whether or not such a gate implementation scheme can be scaled up. The largest PGQC to date with the device architecture discussed in this work has 17 qubits (see Ref. [40]). In order to avoid the problem just discussed, i.e., frequency collisions during the gate, some authors suggest the application of additional flux pules to noninteracting transmon qubits to mitigate the problem (see Sec. 1 in the Supplemental Material of Ref. [16]). Other authors mitigate the issue by redefining the target two-qubit gate (see Ref. [41]) so that the time evolution of the system fits more naturally to the target two-qubit gate.

We emphasize that driving different transmon qubits results in different energy levels being populated and different ELRs being active [see Figs. 4(a)–4(c)]. Consequently, before we can even start building a device, we have to solve an optimization problem of exponential size, i.e., we have to avoid ELRs between all 2^N computational basis states of the NIGQC or PGQC. Note that here we have to take into account different pulse amplitudes δ for the different CZ gates we implement and the different spectra and ELRs which result from driving different transmon qubits. Strictly speaking, our conclusions only apply to the frequency-tunable transmon device architecture studied in this work. However, the consequences of the problem are much more general and are imprinted on many other systems (cf. Refs. [42,43]).

We also emphasize that using microwave pulses to implement single-qubit gates leads to a similar problem, i.e., the MPs are not monochromatic and contain frequency components that can cause unwanted transitions. The more transmon qubits we employ, the more frequency components we have to take into account. If we consider an N-qubit transmon computer, we have to take into account that there are 2^N relevant energy levels and the associated energy differences between these states. Each additional energy difference, i.e., transition frequency, reduces the available frequencies and thus adds to the frequency crowding problem (cf. Ref. [44]).

B. Gate metrics for the elementary gate set

In this section we discuss the results of the control pulse optimization procedure for the three different NIGQCs illustrated in Figs. 1(a)–1(c).

Figures 5(a)–5(d) show the diamond distance $\mu_\diamond$ [Figs. 5(a) and 5(b)] and the average infidelity $\mu_{\mathrm{IF}_{\mathrm{avg}}}$ [Figs. 5(c) and 5(d)] for the two-qubit (in blue), the three-qubit (in green) and the four-qubit (in red) NIGQCS modeled with the circuit Hamiltonian (2) [Figs. 5(a) and 5(c)] and the effective Hamiltonian (7) [Figs. 5(b) and 5(d)]. The results are also listed in Tables XX–XXV in Appendix D. The single-qubit $R^{(x)}(\pi/2)$ rotations are implemented with the MP in Eq. (12). The two-qubit CZ gates are implemented with the UMP in Eq. (13). We use the device parameters listed in Table I and the pulse parameters listed in Tables VIII–XIX to obtain the results (see Appendix D). We employ the algorithms in the open-source NLOPT library (see Ref. [45]) to perform the optimization of the control pulse parameters.

The smallest values for the distance $\mu_\diamond$ and the average infidelity $\mu_{\mathrm{IF}_{\mathrm{avg}}}$ obtained with the circuit Hamiltonian (2) [effective Hamiltonian (7)] are $\mu_\diamond = 0.0080$ and $\mu_{\mathrm{IF}_{\mathrm{avg}}} = 0.0004$ ($\mu_\diamond = 0.0089$ and $\mu_{\mathrm{IF}_{\mathrm{avg}}} = 0.0004$) for the $R_1^{(x)}(\pi/2)$ [$R_0^{(x)}(\pi/2)$] gate and the two-qubit NIGQC. Note that the same gate modeled with the circuit Hamiltonian (2) [effective Hamiltonian (7)] on the four-qubit NIGQC yields $\mu_\diamond = 0.058$ and $\mu_{\mathrm{IF}_{\mathrm{avg}}} = 0.004$ ($\mu_\diamond = 0.060$ and $\mu_{\mathrm{IF}_{\mathrm{avg}}} = 0.004$). Consequently, we lose about one order of magnitude in accuracy by adding additional circuit elements to the system.

The largest values for the distance $\mu_\diamond$ and the average infidelity $\mu_{\mathrm{IF}_{\mathrm{avg}}}$ obtained with the circuit Hamiltonian (2)

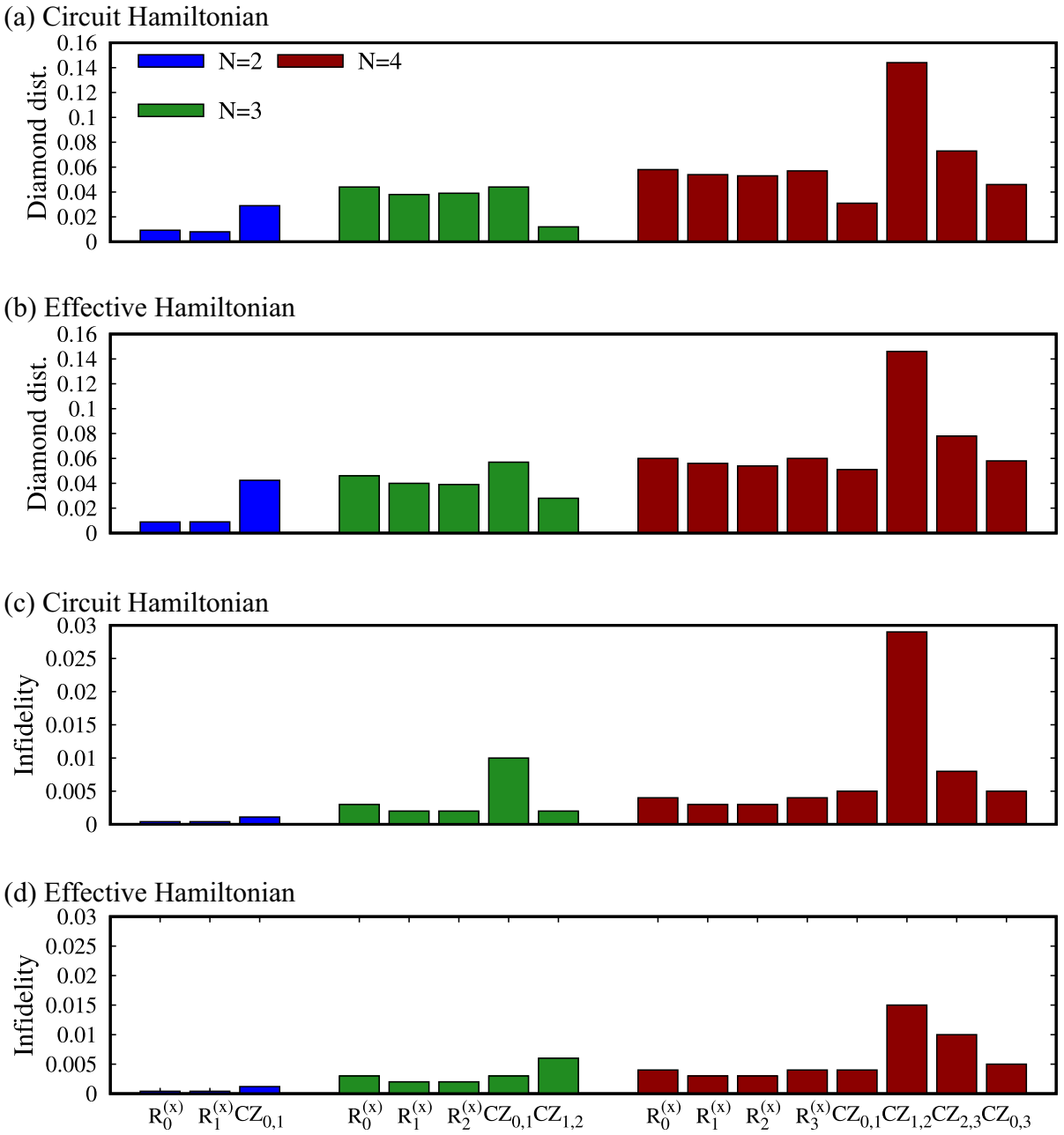

FIG. 5. (a) and (b) Diamond distances $\mu_\diamond$ given by Eqs. (28) and (29) and (c) and (d) average infidelity $\mu_{\mathrm{IF_{avg}}}$ given by Eq. (24) for $R^{(x)}(\pi/2)$ rotations and CZ gates for the NIGQCs illustrated in Figs. 1(a)–1(c), where $N = 2$ in Fig. 1(a), $N = 3$ in Fig. 1(b), and $N = 4$ in Fig. 1(c). The error metrics are obtained with (a) and (c) the circuit Hamiltonian (2) and (b) and (d) the effective Hamiltonian (7). We use the device parameters listed in Table I and the pulse parameters listed in Tables VIII–XIX to obtain the results. The single-qubit $R^{(x)}(\pi/2)$ rotations are obtained with a microwave pulse [see Fig. 2(a)]. The two-qubit CZ gates are obtained with the unimodal pulse [see Fig. 2(b)].

[effective Hamiltonian (7)] are $\mu_\diamond = 0.144$ and $\mu_{\mathrm{IF_{avg}}} = 0.029$ ($\mu_\diamond = 0.146$ and $\mu_{\mathrm{IF_{avg}}} = 0.015$) for the $\mathrm{CZ}_{1,2}$ gate and the four-qubit NIGQC. We can potentially explain the large values for the $\mathrm{CZ}_{1,2}$ gate-error metrics in both models by means of the energy level repulsions in Fig. 4(b). The ELR used to implement the $\mathrm{CZ}_{1,2}$ gate is too close to other ELRs which lead to additional transitions between the states of the system. The optimization algorithm cannot solve this problem. Note that we employ the quite accurate (see Ref. [25] and Appendix B in Ref. [18]) series expansions in Eqs. (B4) and (B7) to model the tunable qubit frequency and anharmonicity, respectively. If we employ the less precise first-order expansions, we cannot reproduce the results for the $\mathrm{CZ}_{1,2}$ gate with the effective model.

Furthermore, in Figs. 5(a)–5(d) we can clearly observe a trend to larger gate-error metrics for larger systems; this is the case for both models. Note that the smallest system contains three circuit elements and the largest system consists of eight circuit elements.

While optimizing the control pulse parameters for the two-qubit gates, we notice that with increasing system size, i.e., the number of transmon qubits and couplers, it becomes more

difficult to pass though the various ELRs in the spectrum sufficiently fast (slow) [see Figs. 4(a)–4(c)]. If we let the pulse flanks [see Fig. 2(b)] rise (fall) too slowly, we pass though various ELRs so slowly that unwanted population exchanges occur. If we let the pulse flanks rise (fall) too fast, we observe what are probably nonadiabatic transitions which can even excite the resonators. Obviously, there exists an analogous problem for drive frequencies $\omega^{(D)}$ of the single-qubit $R^{(x)}(\pi/2)$ rotations since the MP pulses are not strictly monochromatic. Both these problems can potentially explain the tendency to larger gate-error metrics in larger NIGQCs.

Furthermore, we also need to consider the difficult task given to the optimization algorithm. Optimizing the control pulse parameters for an N-qubit NIGQC amounts to aligning the time evolution of the system such that the matrix M given by Eq. (31) with 2^{2N+1} double precision numbers is quasiperfectly aligned with the target matrix U. We do not know of an optimization algorithm that can solve such a task with a guarantee of success.

We also find (data not shown) that we cannot simply use the same optimized control pulse parameters for both the circuit model and the effective model. If we use the parameters of the circuit model for the effective model, we can observe diamond distances and average infidelities close to one. The reason for this is that parameters like the drive frequency $\omega^{(D)}$ ($\hbar\omega^{(D)}$) of the MP pulse and the pulse amplitude δ [$\hbar\omega^{(q)}(\delta)$] of the UMP must be at least fine-tuned up to the sixth decimal (a couple of kilohertz). Also, the values that the optimization algorithm obtains are very sensitive to changes in the model and the model parameters. For example, if the interaction strength G is changed from 300 MHz to 301 MHz, we would already need to restart the whole optimization of the control pulse parameters to obtain gate-error metrics that are not significantly worse than the ones shown in Figs. 5(a)–5(d). Obviously, this lack of robustness can be expected to become even more severe when an actual experiment, instead of a simulation, is conducted.

C. Influence of higher states on gate-error trajectories obtained with the circuit Hamiltonian

In this section we discuss simulation results for the implementation of $R_0^{(x)}(\pi/2)$ gates on the four-qubit NIGQC illustrated in Fig. 1(c), modeled with the circuit Hamiltonian (2) using four and 16 basis states for the transmon qubits. All resonators are modeled with four basis states. Also, we use a fixed set of control pulse parameters for all simulations (see Table XII, row 1, in Appendix D).

In Table II we show the results for two different simulations. In the first (second) case, we simulate the $R_0^{(x)}(\pi/2)$ gate with four (16) basis states for all transmon qubits in the system.

On the one hand, we can observe that the diamond distance $\mu_\diamond$ exhibits an increase in the third decimal. Similarly, the average infidelity $\mu_{\mathrm{IF}_{\mathrm{avg}}}$ increases in the fourth decimal. On the other hand, we can see that the leakage measure μ_{leak} and the statistical distance μ_{SD} (obtained for the NIGQC computational basis state $|0,0,0,0\rangle$) are the same, up the fourth decimal. Note that the leakage measure μ_{leak} and statistical distance μ_{SD} are computed from the squares of the state vector amplitudes only. Consequently, the phase of the system is neglected completely. This makes both these quantifiers less susceptible to changes in the number of basis states.

TABLE II. Error metrics for a four-qubit NIGQC as illustrated in Fig. 1(c). The error metrics are obtained with the circuit Hamiltonian (7), the device parameters listed in Table I, and the pulse parameters listed in Table XII. The first column lists the target gate, the second column the number of basis states used to model the dynamics of the transmons, the third column the diamond distance $\mu_\diamond$ given by Eqs. (28) and (29), the fourth column the average infidelity $\mu_{\mathrm{IF}_{\mathrm{avg}}}$ given by Eq. (24), the fifth column the leakage measure μ_{leak} given by Eq. (26), and the sixth column the statistical distance given by Eq. (17). The statistical distance is obtained for the ground state of the NIGQC.

Gate	States	$\mu_\diamond$	$\mu_{\mathrm{IF}_{\mathrm{avg}}}$	μ_{leak}	μ_{SD}
$R_0^{(x)}(\pi/2)$	4	0.0505	0.0037	0.0024	0.0014
$R_0^{(x)}(\pi/2)$	16	0.0584	0.0040	0.0024	0.0014

Figures 6(a)–6(d) show the diamond distance $\mu_\diamond$ [Fig. 6(a)], the average infidelity $\mu_{\mathrm{IF}_{\mathrm{avg}}}$ [Fig. 6(b)], the leakage measure μ_{leak} [Fig. 6(c)], and the statistical distance μ_{SD} [Fig. 6(d)] as functions of the number of consecutively executed $R_0^{(x)}(\pi/2)$ gates. Furthermore, we obtain the blue solid line when all transmon qubits are modeled with four basis states only. The green dash-dotted line is obtained when all transmon qubits are modeled with 16 basis states.

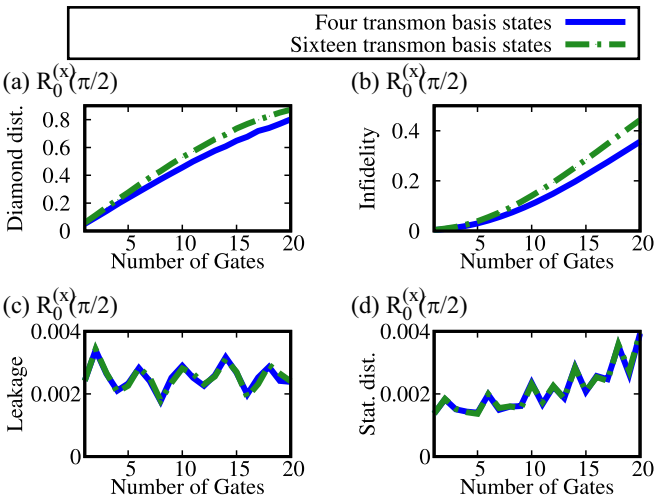

FIG. 6. Gate errors as functions of the number of gates for a program which executes 20 $R^{(x)}(\pi/2)$ in a row for (a) diamond distance, (b) average infidelity, (c) leakage measure, and (d) statistical distance for the initial state $|0,0,0,0\rangle$. We ran the gate sequence on the four-qubit NIGQC illustrated in Fig. 1(c). The results are obtained with the circuit Hamiltonian (2) and the device parameters listed in Table I. We ran the program twice. The first time was with four basis states for every flux-tunable transmon in the system. These results are displayed with blue solid lines. The second time was with 16 basis states for every flux-tunable transmon in the system. These results are displayed with green dash-dotted lines. We observe that the gate-error metrics in (a) and (b) deviate by about 10% after 20 repetitions. The deviations for the gate-error metrics in (c) and (d) are smaller by more than a factor of 100.

The statistical distance μ_{SD} is obtained for the initial state $|0,0,0,0\rangle$ of the NIGQC.

The diamond distance $\mu_\diamond$ [Fig. 6(a)] and the average infidelity $\mu_{\mathrm{IF}_{\mathrm{avg}}}$ [Fig. 6(b)] modeled with four (blue solid line) and 16 (green dash-dotted line) basis states start to deviate after the execution of a couple of $R_0^{(x)}(\pi/2)$ gates. Finally, after 20 $R_0^{(x)}(\pi/2)$ gates we find that the diamond distance $\mu_\diamond$ [Fig. 6(a)] and the average infidelity $\mu_{\mathrm{IF}_{\mathrm{avg}}}$ [Fig. 6(b)] deviate by about 10% for both cases. We also observe that the leakage measure μ_{leak} and the statistical distance μ_{SD} are less affected by changing the number of basis states, i.e., both gate-error quantifiers are roughly the same up to the fourth decimal. Note that usually gates are modeled with two or three basis states only (see, for example, Refs. [9,46–50]).

Finally, we conclude that gate-error metrics obtained with a fixed number of basis states are valid only if the corresponding numerical values have actually converged. Changing the number of basis states can result in a new NIGQC model and there is no guarantee that the gate-error metrics obtained with the new model are the same as for the old model. Thereby we exclude the unlikely case that one can explicitly show that the truncated time-evolution operators [see Eqs. (21) and (31)] for both models are the same. In practice, one has to increase the number of basis states until the results converge to a stable value that is independent of further increase. We followed this procedure for all the results presented in the rest of the paper. However, since in this section the intention is to highlight the relevance of this procedure, we intentionally show results for both four and 16 basis states in Table II and Fig. 6. These results additionally show that some gate-error metrics are less susceptible to changes in the number of basis states and that a growing number of gates might require us to use more basis states to model the dynamics of the system. Interestingly, this type of resilience might also be relevant for experiments in which the higher states may also be substantially different than expected from theory [51].

D. Influence of parameter changes on gate-error trajectories obtained with the circuit Hamiltonian

In this section we discuss simulation results for the implementation of $\mathrm{CNOT}_{0,1} = H_0\mathrm{CZ}_{0,1}H_0$ gate repetition programs executed with the two-qubit, three-qubit, and four-qubit NIGQCs illustrated in Figs. 1(a)–1(c), respectively, modeled with the circuit Hamiltonian (2) and slightly different $\delta + \Delta\delta$ control pulse parameters for the $\mathrm{CZ}_{0,1}$ gates implemented with the UMP given by Eq. (13). In the following, $\Delta\delta$ denotes the offset value. The original control pulse parameters for the UMPs we use to implement the $\mathrm{CZ}_{0,1}$ gates are listed in Tables IX, XI, and XIII, row 1, for the two-, three-, and four-qubit NIGQCs, respectively. All Hadamard H_0 gates are implemented with $R^{(x)}(\pi/2)$ rotations and virtual Z gates. We use the MP given by Eq. (12) and the control pulse parameters listed in Tables VIII, X, and XII, row 1, for the two-, three-, and four-qubit NIGQCs, respectively. Note that for these simulations we do not optimize the circuit by eliminating the H_0 gates. We are interested in how the errors caused by different $\Delta\delta$ interact with the single-qubit rotations. In this section we model the dynamics of the Hamiltonian (2) with 16 basis states for all transmon qubits, except the one with the index $i = 0$ [cf. Figs. 1(a)–1(c)], where we use four basis states. Additionally all resonators are modeled with four basis states only. Table III shows the gate-error quantifiers for the execution of a single $\mathrm{CNOT}_{0,1}$ on the two-qubit NIGQC illustrated in Fig. 1(a). The results are obtained with four slightly different pulse amplitudes $\delta + \Delta\delta$ for the UMP which implements the $\mathrm{CZ}_{0,1}$ gate. We use $\Delta\delta/2\pi = 0$ in row 1, $\Delta\delta/2\pi = 10^{-6}$ in row 2, $\Delta\delta/2\pi = 10^{-5}$ in row 3, and $\Delta\delta/2\pi = 10^{-4}$ in row 4.

TABLE III. Error metrics for a two-qubit NIGQC as illustrated in Figs. 1(a). The error metrics are obtained with the circuit Hamiltonian (7), the device parameters listed in Table I, and the pulse parameters listed in Tables VIII and IX. The first column lists the target gate, the second column the offset value $\Delta\delta$ we use to implement the CZ gates, the third column the diamond distance $\mu_\diamond$ given by Eqs. (28) and (29), the fourth column the average infidelity $\mu_{\mathrm{IF}_{\mathrm{avg}}}$ given by Eq. (24), the fifth column the leakage measure μ_{leak} given by Eq. (26), and the sixth column the statistical distance given by Eq. (17). The statistical distance is obtained for the ground states of the NIGQCs. We employ the UMP given by Eq. (13) to obtain the results.

Gate	$\Delta\delta/2\pi$	$\mu_\diamond$	$\mu_{\mathrm{IF}_{\mathrm{avg}}}$	μ_{leak}	μ_{SD}
$\mathrm{CNOT}_{0,1}$	0	0.0386	0.0018	0.0012	0.0013
$\mathrm{CNOT}_{0,1}$	10^{-6}	0.0390	0.0018	0.0012	0.0013
$\mathrm{CNOT}_{0,1}$	10^{-5}	0.0456	0.0022	0.0012	0.0013
$\mathrm{CNOT}_{0,1}$	10^{-4}	0.1594	0.0156	0.0018	0.0038

We observe that the diamond distance $\mu_\diamond$ is affected by the third decimal if we change the pulse amplitude by $\Delta\delta/2\pi = 10^{-6}$. However, for this case the average infidelity $\mu_{\mathrm{IF}_{\mathrm{avg}}}$ is the same up to the fourth decimal. If we consider the offset value $\Delta\delta/2\pi = 10^{-5}$ ($\Delta\delta/2\pi = 10^{-4}$), we find that the diamond distance $\mu_\diamond$ is affected by the second (first) decimal and the average infidelity $\mu_{\mathrm{IF}_{\mathrm{avg}}}$ is affected by the third (second) decimal.

If we consider the flux-tunable qubit frequency of the transmon qubit we drive [see $\omega_1^{(Q)}$ in Fig. 1(a)], we find that keeping the pulse amplitude stable up to the sixth (fourth) decimal, for the offset $\Delta\delta/2\pi = 10^{-6}$, means controlling the flux-tunable qubit frequency up to a couple of kilohertz (megahertz). For this estimate of the energy scale we consider the spectrum of the corresponding circuit Hamiltonian with the device parameters listed in Table I, row $i = 1$.

Figures 7(a)–7(f) show the diamond distance $\mu_\diamond$ [Figs. 7(a), 7(c), and 7(e)] and the infidelity $\mu_{\mathrm{IF}_{\mathrm{avg}}}$ [Figs. 7(b), 7(d), and 7(f)] as functions of the number of gates for the two-qubit [Figs. 7(a) and 7(b)], three-qubit [Figs. 7(c) and 7(d)], and four-qubit [Figs. 7(e) and 7(f)] NIGQCs illustrated in Figs. 1(a)–1(c). Here we executed a gate sequence which contains 20 controlled-NOT (CNOT) gates in a row on the different NIGQCs. In each panel we show the results for four different offsets: $\Delta\delta/2\pi = 0$ (blue solid line), $\Delta\delta/2\pi = 10^{-6}$ (green dash-dotted line), $\Delta\delta/2\pi = 10^{-5}$ (red dotted line), and $\Delta\delta/2\pi = 10^{-4}$ (violet solid line). Note that each CNOT gate is implemented with two MPs and one UMP and we do not remove the H_0 gates from the circuit.

We observe that the qualitative and quantitative behaviors of the gate-error trajectories barely change for the offset $\Delta\delta/2\pi = 10^{-6}$; small deviations only become noticeable at

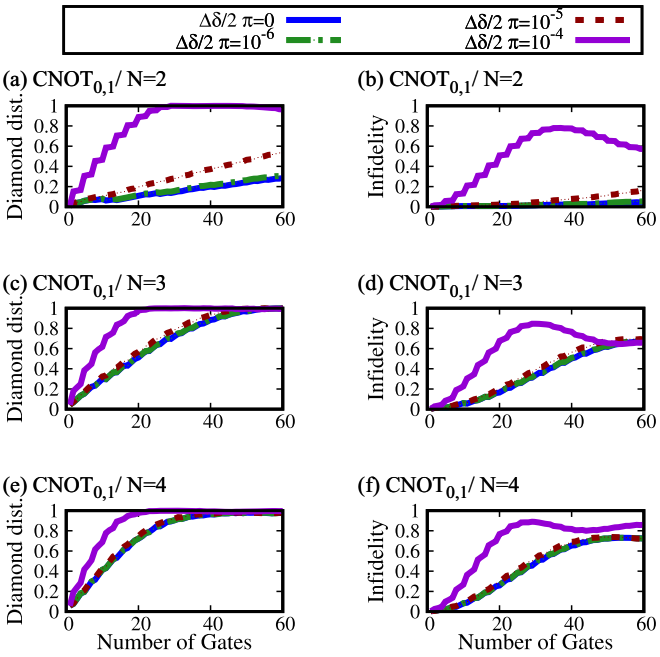

FIG. 7. Gate errors as functions of the number of gates for a program which executes 20 CNOT gates in a row for (a), (c), and (e) diamond distance and (b), (d), and (f) average infidelity. Note that every CNOT gate is implemented with one UMP pulse and two MP pulses. The program is run on (a) and (b) the two-qubit NIGQC with $\mathrm{CNOT}_{0,1}$ and $N = 2$, (c) and (d) the three-qubit NIGQC with $\mathrm{CNOT}_{0,1}$ and $N = 3$, and (e) and (f) the four-qubit NIGQC with $\mathrm{CNOT}_{0,1}$ and $N = 4$. The two-, three-, and four-qubit systems are illustrated in Figs. 1(a)–1(c), respectively. The results are obtained with the circuit Hamiltonian (2) and the device parameters listed in Table I. We run the program four times on each NIGQC. Each time we added an offset $\Delta\delta$ to the pulse amplitude δ of the UMP which implements the CZ gates. The results for the offset $\Delta\delta/2\pi = 0$, 10^{-6}, 10^{-5}, and 10^{-4} are shown with blue solid, green dashed, red dotted, and violet solid lines, respectively. For the offset $\Delta\delta/2\pi = 10^{-4}$ we can observe some type of tipping behavior, i.e., the gate-error trajectory changes its form completely [see (a), (b), (d), and (f)]. Also, we observe interesting nonlinear behavior for the gate-error trajectories which are generated by the CNOT sequence.

the end of the repetition program. Once we increase the offset to $\Delta\delta/2\pi = 10^{-5}$, we find that the qualitative and quantitative behaviors of the gate-error trajectories can be affected after a couple of gates. If we consider the offset to $\Delta\delta/2\pi = 10^{-4}$, we can see some type of tipping behavior in all panels, in the sense that the qualitative and quantitative behaviors of the gate-error trajectories can change in a nonlinear manner. Note that one can obtain similar results by adding a frequency offset $\Delta\omega^{(D)}$ to the drive frequency $\omega^{(D)}$ of the single-qubit gate control pulse in Eq. (12).

Finally, we conclude that the stability of the gate-error metrics in our circuit Hamiltonian NIGQC model depends on our ability to control the flux-tunable qubit frequencies (the pulse amplitudes) up to a couple of kilohertz ($\Delta\delta/2\pi = 10^{-6}$). Note that if we execute circuits which contain CZ gates, e.g., $\mathrm{CZ}_{0,1}$, $\mathrm{CZ}_{1,2}$, $\mathrm{CZ}_{2,3}$, and $\mathrm{CZ}_{0,3}$, on different qubits and the corresponding UMPs are affected by the same offset $\Delta\delta$, then the system can become much more sensitive with regard to the offset value $\Delta\delta$, in comparison with the data [see Figs. 7(a)–7(f)] we discussed before.

We can convert the offset factor $\Delta\delta/2\pi = 10^{-6}$ for the flux $\Delta\Phi = (\Phi_0\Delta\varphi)/2\pi$ from webers to teslas for an area of 10×10 $\mu\mathrm{m}^2$, which is characteristic of a flux-tunable transmon (see Ref. [52]). Using the circuit Hamiltonian (2) to simulate NIGQCs, we find that the gate-error metrics are sensitive to field strengths of about 10^{-11} T. Here we assume that the external flux is given by $\Phi = |B|A$, where $|B|$ is the magnetic-field strength and A is the area of the surface, where the flux is threading through. For comparison, the earth's magnetic-field strength is about 10^{-5} T.

Furthermore, the data presented in this section suggest that in our NIGQC model the gate-error metrics obtained for a single gate cannot be used to predict how the gate-error metrics behave in the future. Consequently, the future behavior of a gate-error trajectory is not determined only by its initial value. We can explain this finding in very simple terms. The future state of the system $|\Psi(t)\rangle$ is governed by the time-dependent Schrödinger equation given by Eq. (1) and not by the value of the gate-error metric μ_x itself (x is a label for an arbitrary gate-error metric). Therefore, there is no reason why gate-error metrics suffice to allow a prediction of the time evolution. They are at most a measure of closeness at one particular point in time, i.e., a snapshot of the state of the system.

E. Influence of the adiabatic approximation on gate-error trajectories obtained with the effective Hamiltonian

In this section we discuss simulation results for the implementation of $\mathrm{CZ}_{0,1}$ and $\mathrm{CNOT}_{0,1} = H_0\mathrm{CZ}_{0,1}H_0$ gate repetition programs executed with the two-qubit, three-qubit, and four-qubit NIGQCs illustrated in Figs. 1(a)–1(c), modeled with the effective Hamiltonian (7) in the adiabatic and the nonadiabatic regime. In the adiabatic regime we set the time derivative $\dot{\varphi}(t)$ of the external flux to zero such that the drive term in Eq. (10) is set to zero too. In the nonadiabatic regime, we do not make this assumption, i.e., we model the flux-tunable transmons as nonadiabatic anharmonic oscillators in the harmonic basis. For our simulations, we use four basis states for all transmons and resonators in the model.

For our simulations we employ the UMP [see Fig. 2(b)] given by Eq. (13) and the BMP [see Fig. 2(c)] given by Eq. (14) to test whether or not it is appropriate to model flux-tunable transmons in the adiabatic regime, as it is commonly done in the literature (see, e.g., Refs. [9,28,42,46,48–50,53]). The results for the UMP (BMP) are presented in Table IV (Table V) and Figs. 8(a)–8(l) [Figs. 9(a)–9(l)]. Note that the BMP in Fig. 2(c) shows a fast falling flank at around half of the pulse duration. Consequently, we expect that the deviations between the adiabatic and nonadiabatic cases are larger for the BMP. Furthermore, the UMP and BMP are characterized by long time intervals of about 80 ns where the derivative $\dot{\varphi}(t)$ of the external flux is zero in both models. Consequently, the deviations between the adiabatic and nonadiabatic models should originate from the pulse flanks we can see in Figs. 2(b) and 2(c).

The control pulse parameters for the UMPs and BMPs we use to implement the $\mathrm{CZ}_{0,1}$ gates are listed in Tables XV, XVII, and XIX, rows 1 and 2, for the two-, three-, and four-qubit

TABLE IV. Error metrics for a two-qubit, a three-qubit, and a four-qubit NIGQC as illustrated in Figs. 1(a)–1(c), respectively. The error metrics are obtained with the effective Hamiltonian (7), the device parameters listed in Table I, and the pulse parameters listed in Tables XV, XVII, and XIX. The first column lists the target gate; the second column the model we use to describe the flux-tunable transmons, i.e., the adiabatic or the nonadiabatic model; the third column the diamond distance $\mu_\diamond$ given by Eqs. (28) and (29); the fourth column the average infidelity $\mu_{\mathrm{IF}_{\mathrm{avg}}}$ given by Eq. (24); the fifth column the leakage measure μ_{leak} given by Eq. (26); and the sixth column the statistical distance given by Eq. (17). The statistical distance is obtained for the ground states of the NIGQCs. Here we use the unimodal pulse given by Eq. (13) to obtain the results.

Gate	Adiabatic	System	$\mu_\diamond$	$\mu_{\mathrm{IF}_{\mathrm{avg}}}$	μ_{leak}	μ_{SD}
$\mathrm{CZ}_{0,1}$	yes	Fig. 1(a)	0.0424	0.0012	0.0005	0.0012
$\mathrm{CZ}_{0,1}$	no	Fig. 1(a)	0.0425	0.0012	0.0005	0.0012
$\mathrm{CZ}_{0,1}$	yes	Fig. 1(b)	0.0569	0.0033	0.0017	0.0026
$\mathrm{CZ}_{0,1}$	no	Fig. 1(b)	0.0574	0.0033	0.0017	0.0026
$\mathrm{CZ}_{0,1}$	yes	Fig. 1(c)	0.0514	0.0040	0.0028	0.0025
$\mathrm{CZ}_{0,1}$	no	Fig. 1(c)	0.0509	0.0040	0.0028	0.0025

NIGQCs, respectively. All H_0 gates are implemented with $R^{(x)}(\pi/2)$ rotations and virtual Z gates. We employ the MP

TABLE V. Error metrics for a two-qubit, a three-qubit, and a four-qubit NIGQC as illustrated in Figs. 1(a)–1(c), respectively. The error metrics are obtain with the effective Hamiltonian (7), the device parameters listed in Table I, and the pulse parameters listed in Tables XV, XVII, and XIX. The rows and columns show the same unitless quantities as in Table IV. Here we use the bimodal pulse given by Eq. (14) to obtain the results.

Gate	Adiabatic	System	$\mu_\diamond$	$\mu_{\mathrm{IF}_{\mathrm{avg}}}$	μ_{leak}	μ_{SD}
$\mathrm{CZ}_{0,1}$	yes	Fig. 1(a)	0.0167	0.0006	0.0005	0.0004
$\mathrm{CZ}_{0,1}$	no	Fig. 1(a)	0.0195	0.0007	0.0005	0.0004
$\mathrm{CZ}_{0,1}$	yes	Fig. 1(b)	0.0306	0.0042	0.0036	0.0020
$\mathrm{CZ}_{0,1}$	no	Fig. 1(b)	0.0336	0.0042	0.0035	0.0019
$\mathrm{CZ}_{0,1}$	yes	Fig. 1(c)	0.0415	0.0043	0.0035	0.0024
$\mathrm{CZ}_{0,1}$	no	Fig. 1(c)	0.0435	0.0044	0.0035	0.0024

given by Eq. (12) and the control pulse parameters listed in Tables XIV, XVI, and XVIII, row 1, for the two-, three-, and four-qubit NIGQCs, respectively.

Table IV shows the gate-error quantifiers for the execution of a single $\mathrm{CZ}_{0,1}$ on the two-qubit (rows 1 and 2), three-qubit (rows 3 and 4), and four-qubit NIGQCs (rows 5 and 6) illustrated in Figs. 1(a)–1(c). We implement the CZ gates with UMPs. The odd (even) row numbers show the results

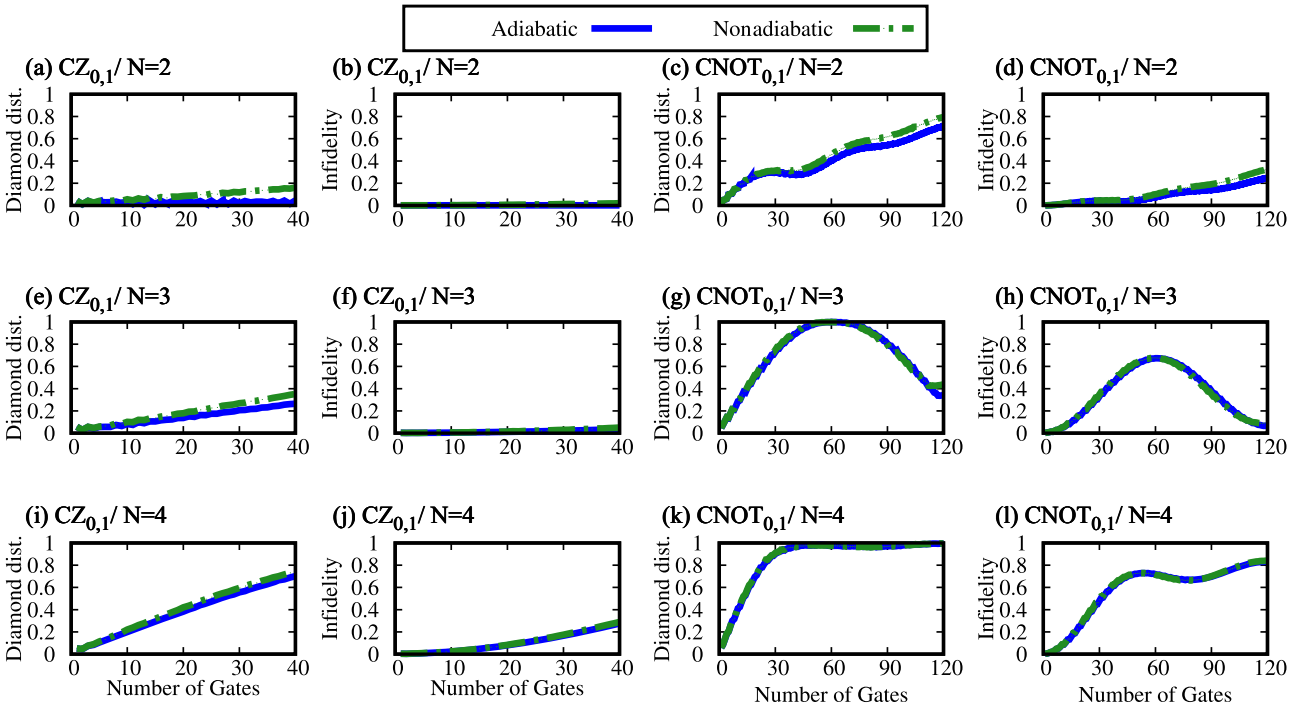

FIG. 8. Gate errors as functions of the number of gates for a program which executes (a), (b), (e), (f), (i), and (j) 40 CZ gates in a row ($\mathrm{CZ}_{0,1}$) and (c), (d), (g), (h), (k), and (l) 40 CNOT gates in a row ($\mathrm{CNOT}_{0,1}$) for (a), (c), (e), (g), (i), and (k) diamond distance and (b), (d), (f), (h), (j), and (l) average infidelity. Note that every CNOT gate is implemented with one UMP pulse and two MP pulses. We run the program on (a)–(d) the two-qubit NIGQC ($N = 2$), (e)–(h) the three-qubit NIGQC ($N = 3$), and (i)–(l) the four-qubit NIGQC ($N = 4$). The two-, three-, and four-qubit systems are illustrated in Figs. 1(a)–1(c), respectively. The results are obtained with the effective Hamiltonian (2) and the device parameters listed in Table I. We run the program two times on each NIGQC. On the first run, we model the flux-tunable transmons as adiabatic qubits. These results are displayed with blue solid lines. On the second run, we model the flux-tunable transmons as nonadiabatic qubits. These results are displayed with green dash-dotted lines. We can observe that the gate-error trajectories for the two cases can deviate up to 20% for the diamond distance and 10% for the average infidelity. Moreover, we can observe a variety of interesting nonlinear behavior for the gate-error trajectories which are generated by the CNOT program.

for the model in the adiabatic (nonadiabatic) regime. If we compare both cases for the different systems, we observe that the numerical values for the gate-error metrics and measure are nearly all the same except the ones for the diamond distance $\mu_\diamond$, where we observe changes in the fourth and third decimals.

Figures 8(a)–8(l) show the diamond distance $\mu_\diamond$ [Figs. 8(a), 8(e), 8(i), 8(c), 8(g), and 8(k)] and the average infidelity $\mu_{\mathrm{IF}_{\mathrm{avg}}}$ [Figs. 8(b), 8(f), 8(j), 8(d), 8(h), and 8(l)] as functions of the number of gates for the two-qubit [Figs. 8(a)–8(d)], three-qubit [Figs. 8(e)–8(h)], and four-qubit [Figs. 8(i)–8(l)] NIGQCs illustrated in Figs. 1(a)–1(c). Here we executed programs which contain 40 CZ [Figs. 8(a), 8(b), 8(e), 8(f), 8(i), and 8(j)] and 40 CNOT [Figs. 8(c), 8(d), 8(g), 8(h), 8(k), and 8(l)] gates in a row on the different NIGQCs. As in Sec. IV D, we do not remove the H_0 gates from the circuit sequence to study how the errors of the CZ gates interact with the errors of the H gates. In each panel we show the results for the two different cases: The adiabatic regime (blue solid line) and the nonadiabatic regime (green dash-dotted line). Note that each CNOT gate is implemented with two MPs and one UMP, which results in 120 gates in total.

If we consider Figs. 8(a)–8(d) for the two-qubit NIGQC described by the effective Hamiltonian (7), we find that the small deviations between rows 1 and 2 in Table IV can still affect the time evolution of the system such that the gate-error trajectories for the adiabatic and nonadiabatic models begin to diverge over time. Additionally, if we consider the results in Figs. 8(e)–8(l), we also observe that the qualitative and quantitative behaviors of the gate-error trajectories can simply be affected by the presence of additional circuit elements. Note that we execute the same programs on NIGQCs of increasing size and that the device parameters in Table I for the first two transmon qubits and the coupling resonator do not change. However, each time we increase the size of the system we have to optimize the pulse parameters again. Therefore, if we consider the results presented in Sec. IV D, we expect qualitative and quantitative changes in the behavior of the gate errors once we add additional circuit elements to the system and repeat the pulse optimization. Moreover, we observe that the gate-error trajectories for the CZ and CNOT programs show substantially different qualitative and quantitative behaviors even though the deviations between the adiabatic and nonadiabatic cases seem to be of the same order.

Overall, we find fair qualitative agreement for the adiabatic and nonadiabatic cases. The UMPs we model in this work are quite long compared to instances which can be found in the literature (see, for example, Ref. [53]). Therefore, we emphasize that one cannot generalize the results presented in this section and argue that neglecting the nonadiabatic drive term in Eq. (10) is valid for all UMPs.

Table V shows the gate-error quantifiers for the execution of a single $\mathrm{CZ}_{0,1}$ on the two-qubit (rows 1 and 2), three-qubit (rows 3 and 4), and four-qubit NIGQCs (rows 5 and 6) illustrated in Figs. 1(a)–1(c). We implement the CZ gates with BMPs. As before, the odd row numbers show the results for the model in the adiabatic regime and the even row number show the results for nonadiabatic regime. If we compare both cases for the different systems, we notice that the numerical values for the diamond distance $\mu_\diamond$ show deviations in the third decimal. Furthermore, the numerical values for some of the average infidelities $\mu_{\mathrm{IF}_{\mathrm{avg}}}$ show deviations in the fourth decimal. The leakage measure μ_{leak} and the statistical distance μ_{SD} are affected in only one case (see rows 3 and 4).

Figures 9(a)–9(l) show the diamond distance $\mu_\diamond$ [Figs. 9(a), 9(e), 9(i), 9(c), 9(g), and 9(k)] and the infidelity $\mu_{\mathrm{IF}_{\mathrm{avg}}}$ [Figs. 9(b), 9(f), 9(j), 9(d), 9(h), and 9(l)] as functions of the number of gates for the two-qubit [Figs. 9(a)–9(d)], three-qubit [Figs. 9(e)–9(h)], and four-qubit [Figs. 9(i)–9(l)] NIGQCs illustrated in Figs. 1(a)–1(c). We execute programs which contain 40 CZ [Figs. 9(a), 9(b), 9(e), 9(f), 9(i), and 9(j)] and 40 CNOT [Figs. 9(c), 9(d), 9(g), 9(h), 9(k), and 9(l)] gates in a row on the different NIGQCs. As before, we do not remove the H_0 gates from the circuit sequence to study how the errors of the CZ gates interact with the errors of the H gates. In each panel we show the results for the two different cases: The adiabatic regime (blue solid line) and the nonadiabatic regime (green dash-dotted line).

In Figs. 9(a)–9(l) we see that the small numerical deviations in the third and fourth decimals for the gate-error metrics listed in Table V can over time result in substantial changes in the qualitative and quantitative behaviors of the gate-error trajectories which result from modeling transmon qubits in the adiabatic regime. Furthermore, we find that overall the deviations between the adiabatic and nonadiabatic models are much larger than for the case where we implement the CZ gates with UMPs instead of BMPs. Note that the BMP and UMP in Figs. 2(b) and 2(c) are very similar except for the large pulse flank in the middle of the BMP pulse. If we compare Figs. 8(a)–8(d) and Figs. 9(a)–9(d), we also find that the qualitative and quantitative behaviors of the gate-error trajectories are not the same if we model them with different pulses. However, this is not surprising since in Sec. IV D we have already seen that gate-error trajectories are also very sensitive to changes in the model parameters and both sets of pulse parameters were optimized independently, i.e., this can potentially explain why we see these substantial differences.

We emphasize that we have selected data which highlight the small border between the adiabatic and nonadiabatic regimes. In Appendix C we show the results for a different device architecture, which is discussed in Refs. [46,48,49,54], for which the results obtained with the two different models deviate much more. Furthermore, the authors of Ref. [9] used an adiabatic effective model to describe a flux-driven two-qubit system which consists of two transmon qubits and a coupling resonator. Here bimodal flux pulses with much shorter gate durations are considered. The data presented in this section suggest that the corresponding numerical results change once the flux drive term in Eq. (10) is part of the effective model. The reader may recall that in this section we considered only one approximation, i.e., assumption, which simplifies the model Hamiltonian. Most of the effective Hamiltonians used are the result of numerous approximations.

Finally, we conclude that it is not possible to decide beforehand whether or not an approximation, i.e., an assumption which affects the time evolution of the system, is justified when it comes to modeling gate-error metrics like the diamond distance or the average infidelity. As before, we exclude the unlikely case that we can explicitly show that the

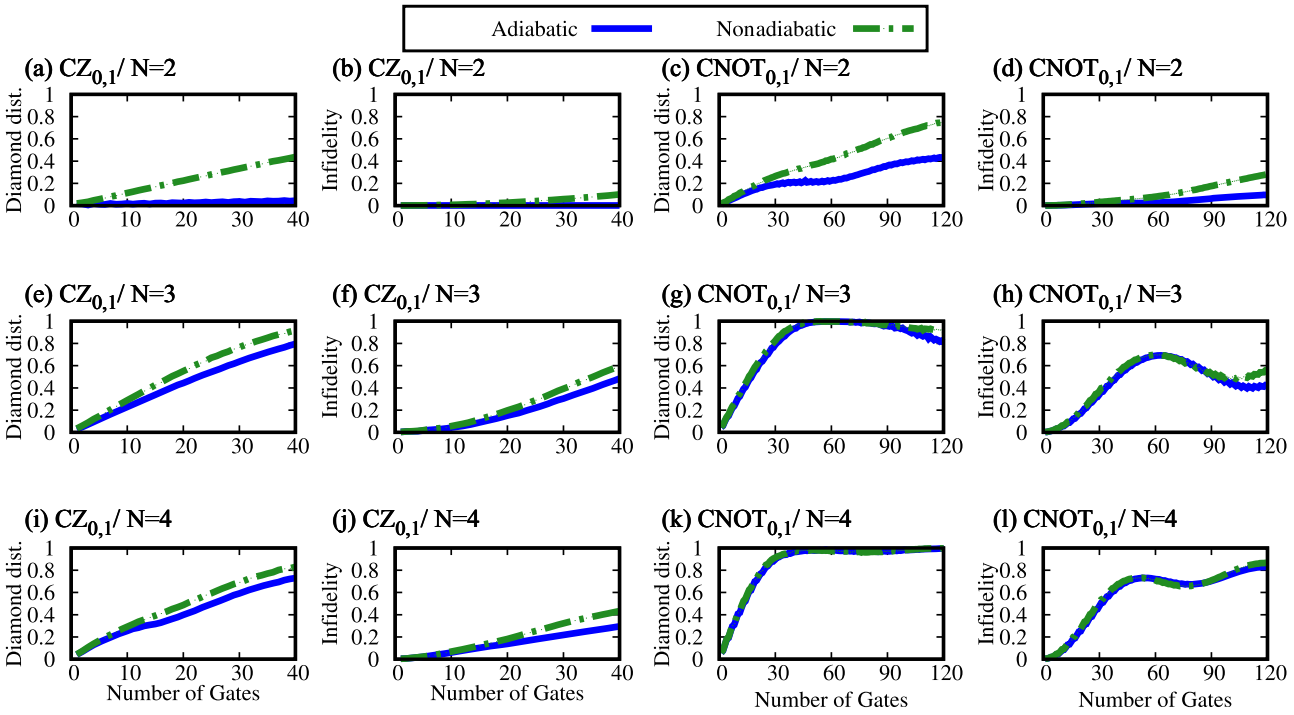

FIG. 9. Gate errors as functions of the number of gates for a program which executes (a), (b), (e), (f), (i), and (j) 40 CZ gates in a row ($CZ_{0,1}$) and (c), (d), (g), (h), (k), and (l) 40 CNOT gates in a row ($CNOT_{0,1}$) for (a), (c), (e), (g), (i), and (k) diamond distance and (b), (d), (f), (h), (j), and (l) average infidelity. Note that every CNOT gate is implemented with one BMP pulse and two MP pulses. We run the program on (a)–(d) the two-qubit NIGQC ($N = 2$), (e)–(h) the three-qubit NIGQC ($N = 3$), and (i)–(l) the four-qubit NIGQC ($N = 4$). The two-, three-, and four-qubit systems are illustrated in Figs. 1(a)–1(c), respectively. The results are obtained with the effective Hamiltonian (2) and the device parameters listed in Table I. We run the program two times on each NIGQC. On the first run, we model the flux-tunable transmons as adiabatic qubits. These results are displayed with blue solid lines. On the second run, we model the flux-tunable transmons as nonadiabatic qubits. These results are displayed with green dash-dotted lines. We can observe large qualitative and quantitative deviations for the gate-error trajectories which are generated by the two different models. In addition, we observe a variety of interesting nonlinear behaviors for the gate-error trajectories which are generated by the CZ and CNOT programs.

truncated time-evolution operators [see Eqs. (21) and (31)] for both models are the same. Consequently, every approximation (assumption) constitutes a new NIGQC model and we do not know whether or not the old reference model yields the same gate-error metrics. The data discussed in this section lead to the conjecture that the quantitative and qualitative behaviors of gate-error trajectories are not simply given by the sum of the individual gate-errors but emerge due to a complex interplay of small deviations with respect to the target gates which occur over time (cf. Refs. [55–57]). Note that the Hamiltonians [see Eq. (7)] for the adiabatic and nonadiabatic cases deviate only for small periods of time and that the gate errors for the different models gradually diverge over time and in the end might show substantially different qualitative and quantitative behaviors.

Furthermore, as in Sec. IV D, the data presented in this section suggest that in our NIGQC models the gate-error metrics obtained for a single gate cannot be used to predict how the gate-error metrics for the next gates in the gate sequence (the program) behave. Consequently, the future behavior of a gate-error trajectory is determined not only by its initial value. As before, we can explain this finding as follows. The future state of the system $|\Psi(t)\rangle$ is still governed by the time-dependent Schrödinger equation given by Eq. (1) and not the value of the gate-error metric itself. Consequently, there is no reason why gate-error metrics should allow a prediction of the time evolution of the system beforehand. Note that we can clearly observe a divergence between the two types of NIGQC models we studied in this section.

V. CONCLUSION

We have studied the gate-error trajectories which arise if one repeats a gate several times in a row. For the simulations we modeled two-qubit, three-qubit, and four-qubit superconducting nonideal gate-based transmon quantum computers, or nonideal gate-based quantum computers for short [see Sec. I and Figs. 1(a)–1(c)]. The time evolution of the state vector $|\Psi(t)\rangle$, which by assumption completely determines the state of a NIGQC, is generated by the time-dependent Schrödinger equation for a time-dependent Hamiltonian $\hat{H}(t)$. We used the circuit Hamiltonian (2) and the associated effective Hamiltonian (7) to generate the dynamics of the systems. The control pulses discussed in Sec. II C were used to implement two types of gates. We used the microwave pulse in Eq. (12) [see Fig. 2(a)] to implement the single-qubit $R^{(x)}(\pi/2)$ rotations. We also implemented CZ gates. We used either the unimodal pulse in Eq. (13) [see Fig. 2(b)] or the bimodal pulse in Eq. (14) [see Fig. 2(c)]. This allowed us to compute various gate-error metrics like the diamond

distance and the average infidelity as functions of the number of gates executed on the NIGQCs. For the computations we implemented the product-formula algorithms to solve the time-dependent Schrödinger equation (see Ref. [58]), the algorithms discussed in Ref. [59] to determine the state $|\psi\rangle$ of the ideal gate-based quantum computer, and the open-source library NLOPT (see Ref. [45]) to optimize the control pulse parameters. The complete simulation software except for the optimization algorithms was developed and implemented in house. The main results in this manuscript were presented in Sec. IV. All results in this work were obtained with the device parameters listed in Table I.

In Sec. IV A we discussed the spectrum of the four-qubit NIGQC illustrated in Fig. 1(c) and its relevance for the implementation of two-qubit CZ gates. We modeled the system with the circuit Hamiltonian (2) and discussed how the complexity of the energy levels, which increases with the system size, i.e., the number of transmon qubits and couplers, can affect the gate-error metrics of the two-qubit CZ gates that we considered. Furthermore, this problem also affects the scaling-up capabilities of the device architecture discussed in this work.

In Sec. IV B we discussed the results of the control pulse optimization (see Fig. 5 and Tables XX–XXV). The corresponding control pulse parameters are listed in Tables VIII–XIX in Appendix D. We found that the gate-error metrics have a tendency to grow with the system size and that we can explain this tendency by studying the energy spectrum of the system [see, for example, Figs. 4(a)–4(c)] and by assessing the difficult task we present to the optimization algorithms that we need to use.

In Sec. IV C we studied a simple sequence which consists of 20 single-qubit $R^{(x)}(\pi/2)$ gates on a four-qubit NIGQC [see Fig. 1(c)]. We modeled the system by the circuit Hamiltonian (2) and computed gate-error metrics with four and 16 basis states for every flux-tunable transmon in the system. The results are displayed in Figs. 6(a)–6(d). We found that after 20 repetitions the diamond distances and the average infidelities computed with different numbers of basis states deviate by about 10%. Moreover, we also saw that the deviations for the leakage error measure and the statistical distances are smaller by about a factor of 100. This can potentially be explained by the fact that these gate-error quantifiers are computed from the squares of the state vector amplitudes only. Note that gates are often modeled with two or three basis states only (see, for example, Refs. [9,46–50]).

In Sec. IV D we studied a sequence which consists of 20 CNOT gates on a two-qubit, a three-qubit, and a four-qubit NIGQC [see Figs. 1(a)–1(c), respectively]. The results were shown in Figs. 7(a)–7(f). We modeled the system by the circuit Hamiltonian (2) and used the UMP given by Eq. (13) [see Fig. 2(b)] to implement the CZ gates. We repeated the simulations four times and added the offsets $\Delta\delta/2\pi \in \{0, 10^{-6}, 10^{-5}, 10^{-4}\}$ to the calibrated control pulse amplitudes δ which implement the CZ gates. The parameters can be found in the first rows of Tables IX, XI, and XI. We found that the gate-error metrics are affected, to some extent, by all three nonzero offset values $\Delta\delta$. We also noticed some type of tipping behavior for the offset factor $\Delta\delta/2\pi = 10^{-4}$, i.e., the qualitative and qualitative behaviors of the gate-error trajectories changed drastically for this offset. This was the case for all three systems [see Figs. 1(a)–1(c)]. If we converted the offset factor $\Delta\delta/2\pi = 10^{-6}$ for the flux $\Delta\Phi = (\Phi_0\Delta\varphi)/2\pi$ from webers to teslas for an area of 10×10 μm^2, which is characteristic for a flux-tunable transmon (see Ref. [52]), we found that the gate-error metrics in NIGQCs modeled with the circuit Hamiltonian (2) were sensitive to field strengths of about 10^{-11} T. For reasons of comparison, we stated that the earth's magnetic-field strength is about 10^{-5} T strong. Additionally, we found that the gate-error trajectories which are generated by the circuit Hamiltonian (2) and the time-dependent Schrödinger equation exhibit interesting nonlinear behavior.

In Sec. IV E we presented results for sequences of 40 CZ and 40 CNOT gates on two-qubit, three-qubit, and four-qubit NIGQCs. The results were shown in Figs. 8(a)–8(l) and Figs. 9(a)–9(l). We modeled the system with the effective Hamiltonian (7) and used the UMP to obtain the results in Figs. 8(a)–8(l) and the bimodal pulse to obtain the results in Figs. 9(a)–9(l). We ran the CZ and CNOT sequences on two different types of NIGQCs. On the first type of NIGQC the flux-tunable transmons were modeled adiabatically, i.e., we set the time derivative $\dot{\varphi}(t) = 0$ of the external flux, which was used to implement the CZ gates, to zero. On the second type of NIGQC we modeled all flux-tunable transmons nonadiabatically. Although the UMP we used seemingly justified the adiabatic approximation [see Fig. 2(b)], we found that the results for the diamond distance can vary up to 0.2 and the results for the average fidelity up to 0.1. In addition, in most cases the qualitative behavior of the gate-error trajectory was not affected by the adiabatic approximation for the UMP. The bimodal pulses we used do not seem to justify making the adiabatic approximation [see Fig. 2(c)] and in fact we found that the corresponding gate-error trajectories for the adiabatic and nonadiabatic cases showed strong qualitative and quantitative deviations. Additionally, we also observed that the gate-error trajectories which were generated by the effective Hamiltonian (7) and the time-dependent Schrödinger equation showed interesting nonlinear behavior. Furthermore, we found that the qualitative behaviors of the gate-error trajectories for the CZ and CNOT gates were usually not the same. In fact, often they showed completely different behaviors. Therefore, we suspect that the qualitative behavior of a gate-error trajectory is not simply given by the sum of the individual errors but arises due to a complex interplay of small deviations with respect to the target gates.

The results in Secs. IV B–IV E showed that even seemingly small changes in the model, i.e., in the assumptions we made, can substantially affect the gate-error metrics we compute. The fact itself is not surprising and something one should expect. However, the extent to which the changes affected the gate-error metrics during the course of the time evolution is something worth knowing. Note that in each section we focused on one aspect of the model which affects the computation of gate-error metrics. One can easily imagine what happens if one begins to combine changes in the different aspects of the models, namely, that we cannot determine a root cause anymore.

Based on the data presented in Secs. IV A–IV E, we concluded that almost all assumptions we made about the model

could substantially affect the time evolution of the systems and consequently the gate-error metrics we modeled. Therefore, we advocate the view that every assumption leads to a new independent NIGQC model and we simply cannot estimate how the different assumptions affect the gate-error metrics we model. Again we excluded the unlikely case that we can explicitly show that the truncated time-evolution operators [see Eqs. (21) and (31)] for both models are the same. Therefore, the data presented in this work emphasize the narrow borders between certain NIGQC models. Note that we could have selected other data which show much larger deviations between the various NIGQC models. However, emphasizing the narrow path between two seemingly very similar models also has the benefit of adding evidence to our conjecture that in NIGQC models gate errors for consecutive gates are not simply given by the sum of the gate errors for the individual gates in the program sequence but emerge due to a complex interplay of small deviations with respect to the target gates which occur over time (cf. Refs. [55–57]).

Since we found that nearby values for the diamond distance and the average infidelity for a given target gate can lead to very different qualitative behavior for the gate-error trajectories which arise if we execute the target gate several times, we concluded that the gate-error metrics for a given target gate cannot be used to predict the behavior of the gate-error sequence which emerges over time. Note that we showed this with two different generic model Hamiltonians (2) and (7), i.e., this is not a feature of one particular model. Moreover, if we take into account the results in Refs. [3,29], we also find that this not a feature of one particular device architecture. Consequently, we advocate the view that gate-error metrics are at most snapshots for the state of a system at one particular moment in time and not predictors of the gate errors which emerge over time and/or the performance for complete programs (algorithms) executed on the system. In fact, this shortcoming is something we should expect. The gate-error metrics we computed were derived in the context of the IGQC model. This model is inherently static, i.e., changes in the state of the system are modeled as if they occur instantaneously. However, if the future state of the system is governed by the time-dependent Schrödinger equation, there is no reason why gate-error metrics alone should be able to predict the time evolution of the system. They are at most a measure of closeness at one particular point in time.

This then leads to the following question: How can we actually study gate errors in PGQCs if, in most cases, we cannot conclusively compare two NIGQC models and determine where the differences in the gate-error metrics originate from? In Sec. I we briefly mentioned (see Refs. [9–12,12,60,61]) several problems which plague superconducting PGQCs. The seemingly more complex circuit Hamiltonian (2) was derived on the basis of the lumped-element approximation (see Sec. 1.4 in Ref. [17]) and neglected many of these problems by assumption. Additionally, it is not a trivial task to access the state vector and/or the density operator which is supposed to describe the complete state of a PGQC, also by assumption. Adding this uncertainty to all the other uncertain factors in an experiment, we found ourselves in a position where studying individual gate errors in an actual experiment seems impossible. Therefore, we advocate the view that one should use benchmark protocols like the ones discussed in Refs. [3,4] to assess and/or compare different PGQCs.

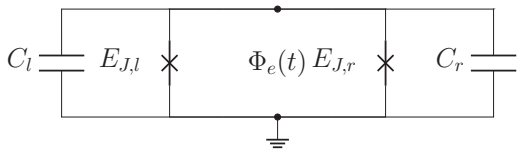

FIG. 10. Illustration of a lumped-element circuit with two linear capacitors with capacitances C_l (left) and C_r (right), two Josephson junctions with Josephson energies $E_{J,l}$ (left) and $E_{J,r}$ (right), and an external flux $\Phi_e(t)$ threading through the central loop. As it is common practice, we mark the ground node by a dashed triangle.

In this work we focused on the execution of simple gate sequences which generate interesting gate-error trajectories for various simulation settings. For future work it might be interesting to see how variational hybrid algorithms such as the quantum approximate optimization algorithm (see Refs. [62,63]) perform on the NIGQCs calibrated for this work.

ACKNOWLEDGMENTS

The authors gratefully acknowledge the Gauss Centre for Supercomputing e.V. for funding this project by providing computing time on the GCS Supercomputer JUWELS [31] at Jülich Supercomputing Centre (JSC). H.L. acknowledges support from the project OpenSuperQ (Grant No. 820363) of the EU Quantum Flagship. D.W. acknowledges partial support by the German Federal Ministry of Education and Research (BMBF), funding program "Quantum technologies – from basic research to market", project Q(AI)^2 (Grant No. 13N15584). H.L., D.W., and M.W. acknowledge support from the project Jülich Unified Infrastructure for Quantum computing, which has received funding from the German Federal Ministry of Education and Research (BMBF) and the Ministry of Culture and Science of the State of North Rhine-Westphalia (MKW NRW).

APPENDIX A: DERIVATION OF A CIRCUIT HAMILTONIAN FOR FLUX-TUNABLE TRANSMONS WITH AN ADDITIONAL CHARGE DRIVE TERM

In the main text we used the circuit Hamiltonian (4) to model flux-tunable transmons with a linear charge drive term. In this Appendix we derive circuit Hamiltonian (4) from the assumptions which constitute the lumped-element approximation (see Sec. 1.4 in Ref. [17]). The external charge variable $n_g(t)$ provides us with a linear drive term which can be used to implement single-qubit gates. Similarly, the external flux variable $\Phi_e(t)$ provides us with a drive term which can be used to implement two-qubit gates. The following derivation is motivated by the work in Ref. [23], i.e., we take into account recent developments in the theory of circuit quantization. Note that the underlying assumptions we use are slightly different from the ones used in Ref. [23]. We use $\hbar = 1$ throughout this work.

We begin with the quantization of the lumped-element circuit illustrated in Fig. 10. Kirchhoff's voltage law yields

$$\Phi_l(t) + \Phi_r(t) = \Phi_e(t) \tag{A1}$$

for the central loop of the circuit. In our lumped-element model, we treat the external flux $\Phi_e(t)$ as an electromotive force (EMF) $\dot{\Phi}_e(t)$.

We intend to express the Lagrangian $\mathcal{L}$ of the system in terms of the variable

$$\Phi(t) = m_l \Phi_l(t) + m_r \Phi_r(t). \tag{A2}$$

Note that the left

$$\Phi_l(t) = \frac{\Phi(t) - m_r \Phi_e(t)}{m_\Delta} \tag{A3}$$

and the right

$$\Phi_r(t) = -\frac{\Phi(t) - m_l \Phi_e(t)}{m_\Delta} \tag{A4}$$

branch flux variables satisfy Eq. (A1) for all $m_l, m_r \in \mathbb{R}$ without further ado. Here $m_\Delta = m_l - m_r$.

If we make use of the relations $V_{C_l} = V_{E_{J_l}}$ and $V_{C_r} = V_{E_{J_r}}$ for the left and right loops in Fig. 10, we can express the Lagrangian as

$$\mathcal{L} = \frac{C_l}{2}\left(\frac{\dot{\Phi}(t) - m_r \dot{\Phi}_e(t)}{m_\Delta}\right)^2 + \frac{C_r}{2}\left(\frac{\dot{\Phi}(t) - m_l \dot{\Phi}_e(t)}{m_\Delta}\right)^2 - U[\Phi(t)], \tag{A5}$$

where the potential energy term $U[\Phi(t)]$ reads

$$U[\Phi(t)] = -E_{J_l} \cos\left(\frac{2\pi}{\Phi_0}\frac{\Phi(t) - m_r \Phi_e(t)}{m_\Delta}\right) - E_{J_r} \cos\left(\frac{2\pi}{\Phi_0}\frac{\Phi(t) - m_l \Phi_e(t)}{m_\Delta}\right). \tag{A6}$$

In the next step we evaluate the squares and neglect all factors proportional to $\dot{\Phi}_e(t)^2$, which ultimately only contribute nonmeasurable global phase factors to the time evolution of the system. The Lagrangian after this step reads

$$\mathcal{L} = \frac{C_\Sigma}{2m_\Delta^2}\dot{\Phi}(t)^2 - \frac{C_l m_r + C_r m_l}{m_\Delta^2}\dot{\Phi}_e(t)\dot{\Phi}(t) - U[\Phi(t)]. \tag{A7}$$

The conjugate variable

$$Q = \frac{C_\Sigma}{m_\Delta^2}\dot{\Phi}(t) - \frac{C_l m_r + C_r m_l}{m_\Delta^2}\dot{\Phi}_e(t) \tag{A8}$$

can be used to obtain the Hamiltonian function

$$H = \frac{m_\Delta^2}{2C_\Sigma}Q^2 + \frac{C_l m_r + C_r m_l}{C_\Sigma}\dot{\Phi}_e(t)Q + U[\Phi(t)] \tag{A9}$$

by means of a Legendre transformation (see Ref. [64]). Here again we neglect all factors which contribute only a nonmeasurable global phase factors to the time evolution of the system.

Finally, we can promote the conjugate variables Φ and Q to the conjugate operators $\hat{\Phi}$ and $\hat{Q}$ and perform the substitutions

$$\hat{\varphi} = \frac{2\pi}{\Phi_0}\hat{\Phi}, \tag{A10a}$$

$$\hat{n} = \frac{1}{2e}\hat{Q}, \tag{A10b}$$

$$\varphi_e(t) = \frac{2\pi}{\Phi_0}\Phi_e(t) \tag{A10c}$$

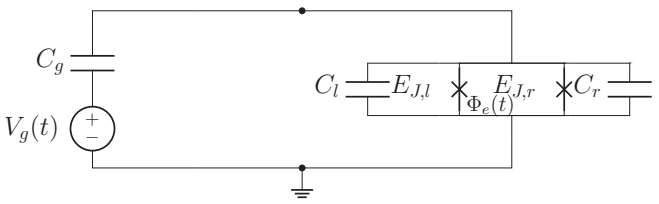

FIG. 11. Illustration of a lumped-element circuit. The right branch contains two linear capacitors with capacitances C_l (left) and C_r (right), two Josephson junctions with Josephson energies $E_{J,l}$ (left) and $E_{J,r}$ (right), and an external flux $\Phi_e(t)$ threading through the loop between the two Josephson junctions. The left branch contains a linear capacitor with capacitance C_g and a voltage source $V_g(t)$. As it is common practice, we mark the ground node by a dashed triangle.

to obtain the Hamiltonian operator

$$\hat{H} = E_{C_\Sigma}\hat{n}^2 + \frac{C_l m_r + C_r m_l}{C_\Sigma}\dot{\varphi}_e(t)\hat{n} + U[\varphi_e(t)]. \tag{A11}$$

Here we made use of $\hbar = 1$. The parametrization of the model can be simplified by assuming $m_\Delta = 1$, $C_l = C_r$, $C_\Sigma = C$, and $m_r = -\beta$. With these assumptions, we can express the Hamiltonian as

$$\hat{H} = E_C\hat{n}^2 + \left(\tfrac{1}{2} - \beta\right)\dot{\varphi}_e(t)\hat{n} + U[\varphi_e(t)]. \tag{A12}$$

The next step in the derivation of the circuit Hamiltonian (4) is to add a linear drive term of the form $n_g(t)\hat{n}$ to the model. In Fig. 11 we display a modified circuit. The circuit shown in Fig. 11 contains an additional branch with a voltage source modeled with the real-valued function $V_g(t)$ and a coupling capacitor with the capacitance C_g. Note that we model the voltage source also as an EMF.

Kirchhoff's voltage law for the central loop

$$V_{C_g} + V_g(t) = V_{C_l} \tag{A13}$$

can be used to obtain the circuit Hamiltonian $\hat{H}^*$ for the system displayed in Fig. 11 by making use of the previously obtained results for the circuit displayed in Fig. 10.

The Lagrangian $\mathcal{L}^*$ of the modified system reads

$$\mathcal{L}^* = \mathcal{L} + \frac{C_g}{2}[\dot{\Phi}_l(t) - V_g(t)]^2. \tag{A14}$$

Therefore, $\mathcal{L}^*$ can also be expressed in terms of the variable $\Phi(t)$. If we evaluate the square in Eq. (A14), we find

$$\mathcal{L}^* = \mathcal{L} + \frac{C_g}{2m_\Delta^2}\Phi(t)^2 - \frac{C_g}{m_\Delta^2}\dot{\Phi}(t)[m_r\dot{\Phi}_e(t) + m_\Delta V_g(t)], \tag{A15}$$

where we neglect all factors which contribute only a nonmeasurable global phase factors to the time evolution of the system. As before, we simplify the parametrization. Assuming $m_\Delta = 1$, $C_l = C_r$, $C = C_\Sigma$, and $m_r = -\beta$ yields

$$\mathcal{L}^* = \frac{C + C_g}{2}\dot{\Phi}(t)^2 - \left(\frac{C}{2} - \beta(C + C_g)\right)\dot{\Phi}_e(t)\dot{\Phi}(t) - C_g V_g(t)\dot{\Phi}(t) - U[\Phi(t)], \tag{A16}$$

where we also neglected factors which in the end contribute only a nonmeasurable global phase factors to the time

evolution of the system. Next, in an *ad hoc* manner, we make the assumption that $C + C_g \to C$ in such a way that the system's time evolution can be modeled with the Lagrangian

$$\mathcal{L}^* = \frac{C}{2}\dot{\Phi}(t)^2 - C\left(\frac{1}{2} - \beta\right)\dot{\Phi}_e(t)\dot{\Phi}(t) - C_g V_g(t)\dot{\Phi}(t) - U[\Phi(t)]. \tag{A17}$$

This allows us to express the conjugate variable as

$$Q = C\dot{\Phi}(t) - C\left(\tfrac{1}{2} - \beta\right)\dot{\Phi}_e(t) - C_g V_g(t). \tag{A18}$$

Consequently, the first part of the Hamiltonian function reads

$$Q\dot{\Phi}(t) = \frac{Q^2}{C} + \left(\frac{1}{2} - \beta\right)\dot{\Phi}_e(t)Q + \frac{C_g}{C}V_g(t)Q \tag{A19}$$

and the second part of the Hamiltonian function can be expressed as

$$\mathcal{L}^* = \frac{Q^2}{2C} - U[\Phi(t)], \tag{A20}$$

where all factors which contribute only a nonmeasurable global phase factors to the time evolution of the system are neglected. Therefore, adding both parts yields

$$H^* = E_C\left(\frac{Q}{2e}\right)^2 + \left(\frac{1}{2} - \beta\right)(2e)\dot{\Phi}_e(t)\left(\frac{Q}{2e}\right) - 2E_C n_g(t)\left(\frac{Q}{2e}\right) + U[\Phi(t)], \tag{A21}$$

where the real-valued function $n_g(t)$ is defined as

$$n_g(t) = -\frac{C_g V_g(t)}{2e}. \tag{A22}$$

As before, we use $\hbar = 1$ to simplify the Hamiltonian.

If we promote the conjugate variables to conjugate operators, complete the square with regard to the external charge variable, make use of the substitutions in Eqs. (A10a)–(A10c), and drop all terms which contribute only nonmeasurable global phase factors to the time evolution of the system, we obtain the result

$$\hat{H}^* = E_C[\hat{n} - n_g(t)]^2 + \left(\tfrac{1}{2} - \beta\right)\dot{\varphi}_e(t)\hat{n} - E_{J,l}\cos[\hat{\varphi} + \beta\varphi_e(t)] - E_{J,r}\cos[\hat{\varphi} + (\beta - 1)\varphi_e(t)]. \tag{A23}$$

In the main text we used the Hamiltonian (A23) to model flux-tunable transmons. Note that in the main text we omitted the labels e and g in the real-valued functions $n_g(t)$ and $\varphi_e(t)$.

APPENDIX B: DETAILED DISCUSSION OF THE EFFECTIVE HAMILTONIAN

In this Appendix we provide a detailed discussion of the effective Hamiltonian (7) we use to obtain the results in Sec. IV E. Note that we use $\hbar = 1$ throughout this work.

The effective Hamiltonian we use to model our NIGQCs is defined as

$$\hat{H}_{\text{eff}} = \hat{H}_{\text{res},\Sigma} + \hat{H}_{\text{tun eff},\Sigma} + \hat{D}_{\text{charge}} + \hat{\mathcal{D}}_{\text{flux}} + \hat{W}_{\text{int}}. \tag{B1}$$

The first term

$$\hat{H}_{\text{res},\Sigma} = \sum_{k\in K}\omega_k^{(R)}\hat{a}_k^\dagger\hat{a}_k \tag{B2}$$

describes a collection of noninteracting resonators. Here $K \subseteq \mathbb{N}^0$ denotes an index set for the resonators and $\omega_k^{(R)}$ refers to the different resonator frequencies. The operators $\hat{a}$ and $\hat{a}^\dagger$ are the bosonic annihilation and creation operators, respectively. We use the basis states of the time-independent harmonic oscillator (see Sec. 2.5 in Ref. [34]) as the basis states for our simulations.

The second term

$$\hat{H}_{\text{tun eff},\Sigma} = \sum_{j\in J}\omega_j^{(q)}(t)\hat{b}_j^\dagger\hat{b}_j + \frac{\alpha_j^{(q)}(t)}{2}[\hat{b}_j^\dagger\hat{b}_j(\hat{b}_j^\dagger\hat{b}_j - \hat{I})] \tag{B3}$$

describes a collection of noninteracting flux-tunable transmons which are modeled as adiabatic, anharmonic oscillators. The operators $\hat{b}$ and $\hat{b}^\dagger$ are the bosonic annihilation and creation operators. The function

$$\omega_j^{(q)}(t) = \sqrt{2E_{C_j}E_{J_{\text{eff},j}}(t)} - \frac{E_{C_j}}{4}\sum_{n=0}^{24}a_n\Xi(t)^n \tag{B4}$$

is used to model the flux-tunable transmon qubit frequency. Here a_n are real-valued constants and E_{C_j} and $E_{J_{\text{eff},j}}(t)$ are the capacitive and effective Josephson energies for the transmon qubits, respectively. The latter is defined as

$$E_{J_{\text{eff},j}}(t) = E_{\Sigma,j}\sqrt{\cos\left(\frac{\varphi_j(t)}{2}\right)^2 + d_j^2\sin\left(\frac{\varphi_j(t)}{2}\right)^2}, \tag{B5}$$

where $d_j = (E_{J_{r,j}} - E_{J_{l,j}})/(E_{J_{r,j}} + E_{J_{l,j}})$. The function $\Xi_j(t)$ in Eq. (B4) is defined as

$$\Xi_j(t) = \sqrt{\frac{E_{C_j}}{2E_{J_{\text{eff},j}}(t)}}. \tag{B6}$$

Furthermore, we define the flux-tunable anharmonicity as

$$\alpha_j^{(q)}(t) = -\frac{E_{C_j}}{4}\sum_{n=0}^{24}b_n\Xi(t)^n, \tag{B7}$$

where the different b_n are real-valued constants. We emphasize that Eqs. (B4) and (B7) are taken from Ref. [25]. The functions in Eqs. (B4) and (B7) are used to approximate the lowest three eigenvalues of the circuit Hamiltonian (4). In Appendix B in Ref. [18] the authors assess and discuss the accuracy of this approximation.

We use the time-dependent harmonic basis states

$$\psi^{(m)}[x(t)] = \frac{1}{\sqrt{2^m m!}}\left(\frac{\xi(t)}{\pi}\right)^{1/4}e^{-x^2(t)/2}\mathcal{H}_m[x(t)] \tag{B8}$$

of the time-dependent harmonic oscillator

$$\hat{H} = E_C\hat{n}^2 + \frac{E_{J,\text{eff}}(t)}{2}[\hat{\varphi} - \varphi_{\text{eff}}(t)]^2 \tag{B9}$$

as the basis states for our simulations of the effective flux-tunable transmons. Additionally, we define the auxiliary functions

$$\xi(t) = \left(\frac{E_{J,\text{eff}}(t)}{2E_C}\right)^{1/2}, \tag{B10a}$$

$$x(t) = \sqrt{\xi(t)}[\varphi - \varphi_{\text{eff}}(t)], \tag{B10b}$$

$$\varphi_{\text{eff}}(t) = \arctan\left[d\tan\left(\frac{\varphi(t)}{2}\right)\right] \tag{B10c}$$

and note that $\mathcal{H}_m$ denotes the Hermite polynomial of order $m \in \mathbb{N}^0$.

The third term

$$\hat{D}_{\text{charge}} = \sum_{j\in J}\Omega_j(t)(\hat{b}_j^\dagger + \hat{b}_j) \tag{B11}$$

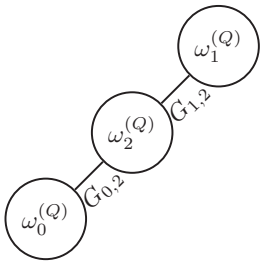

FIG. 12. Illustration of fixed-frequency transmon qubits with qubit frequencies $\omega_0^{(Q)}$ and $\omega_1^{(Q)}$ and a flux-tunable transmon with park frequency $\omega_2^{(Q)}$, which constitute a nonideal gate-based transmon quantum computer with two qubits. The Hamiltonian we use to model the dynamics of our NIGQC is given by Eq. (7). The device parameters we use to specify the Hamiltonian are listed in Table VI. The control pulses we use to implement the gate are given by Eq. (C1).

describes a charge drive. Here $\Omega_j(t) \propto -2E_{C_j} n_j(t)$ and we approximate the charge operators $\hat{n}_j$ by effective charge operators $\hat{n}_{j,\mathrm{eff}}$, which can be expressed in terms of the bosonic annihilation and creation operators (see Ref. [22]).

The fourth term

$$\hat{\mathcal{D}}_{\mathrm{flux}} = \sum_{j\in J} -i\sqrt{\frac{\xi_j(t)}{2}}\dot{\varphi}_{\mathrm{eff},j}(t)(\hat{b}_j^\dagger - \hat{b}_j) + \sum_{j\in J}\frac{i}{4}\frac{\dot{\xi}_j(t)}{\xi_j(t)}(\hat{b}_j^\dagger\hat{b}_j^\dagger - \hat{b}_j\hat{b}_j) \tag{B12}$$

describes a nonadiabatic flux drive. We find

$$\dot{\varphi}_{\mathrm{eff}\,j}(t) = \dot{\varphi}_j(t)\frac{d_j}{2\left[\cos\left(\frac{\varphi_j(t)}{2}\right)^2 + d_j^2\sin\left(\frac{\varphi_j(t)}{2}\right)^2\right]} \tag{B13}$$

and

$$\frac{\dot{\xi}_j(t)}{\xi_j(t)} = \dot{\varphi}_j(t)\frac{\left(d_j^2-1\right)\sin[\varphi_j(t)]}{8\left[\cos\left(\frac{\varphi_j(t)}{2}\right)^2 + d_j^2\sin\left(\frac{\varphi_j(t)}{2}\right)^2\right]}. \tag{B14}$$

The term in Eq. (B12) results from the fact that we model the effective flux-tunable transmon in a time-dependent basis. Therefore, for the time-dependent Schrödinger equation to stay form invariant, a time-dependent basis transformation term is needed (see Ref. [18]).

The fifth term

$$\hat{W}_{\mathrm{int}} = \sum_{(k,j)\in K\times J} g_{k,j}^{(a,b)}(t)(\hat{a}_k^\dagger + \hat{a}_k)\otimes(\hat{b}_j^\dagger + \hat{b}_j) \tag{B15}$$

describes time-dependent dipole-dipole interactions. As before, the time dependence of the interaction strength

$$g_{k,j}^{(a,b)}(t) = G_{k,j}\sqrt[4]{\frac{E_{J_{\mathrm{eff,j}}}(t)}{8E_{C_j}}} \tag{B16}$$

is a result of the fact that we model the effective flux-tunable transmon in a time-dependent basis (see Ref. [18]). This time-dependent interaction strength model is motivated by the work in Ref. [22].

The relation between the effective and the circuit model is discussed in Ref. [18].

TABLE VI. Device parameters for the system illustrated in Fig. 12. The units are the same as for the parameters in Table I. The device parameters are motivated by the experiments discussed in Ref. [54].

i	$\omega_i^{(Q)}/2\pi$	$\alpha_i^{(Q)}/2\pi$	$E_{C_i}/2\pi$	$E_{J_{l,i}}/2\pi$	$E_{J_{r,i}}/2\pi$	$\varphi_{0,i}/2\pi$
0	5.100	−0.310	1.079	13.446	0	0
1	6.200	−0.285	1.027	20.371	0	0
2	8.100	−0.235	0.880	17.905	21.486	0.075

APPENDIX C: SIMULATIONS OF THE PARAMETRIC COUPLER DEVICE ARCHITECTURE

In Sec. IV E we investigated the influence of the adiabatic approximation on gate-error trajectories obtained with the effective Hamiltonian (7) for the device architecture illustrated in Figs. 1(a)–1(c). There the adiabatic approximation was applied to one effective flux-tunable transmon only. In this Appendix we perform analogous simulations for a different device architecture studied in Refs. [46,48,49,54,65]. Here we use a flux microwave pulse to implement two-qubit CZ gates.

The device architecture is illustrated in Fig. 12 and the device parameters are listed in Table VI. The interaction strength G is set to 85 MHz for all simulations (see Appendix B). Here we couple two fixed-frequency transmons with qubit frequencies $\omega_0^{(Q)}$ and $\omega_1^{(Q)}$ by means of a flux-tunable transmon with park frequency $\omega_2^{(Q)}$. We use the control pulse

$$\varphi(t) = \varphi_0 + \delta e(t)\cos(\omega^{(D)}t) \tag{C1}$$

for the external flux $\varphi(t)$ to implement a sequence of CZ gates. The real-valued function $e(t)$ is an envelope function, δ is the pulse amplitude, $\omega^{(D)}$ is the drive frequency, and φ_0 denotes the flux offset. Since the flux offset defines an operating point for the device, we list the parameter in Table VI. The envelope function is defined as

$$e(t) = \begin{cases} \sin(\lambda t) & \text{if } 0 \leqslant t < T_{\mathrm{RF}} \\ 1 & \text{if } T_{\mathrm{RF}} \leqslant t \leqslant \Delta T \\ \sin\left[\frac{\pi}{2} + \lambda(t-\Delta T)\right] & \text{if } \Delta T < t \leqslant T_p, \end{cases} \tag{C2}$$

where T_{RF} denotes the rise and fall time, $\lambda = \pi/2T_{\mathrm{RF}}$, and $\Delta T = T_p - T_{\mathrm{RF}}$. Note that in the computer program we add an additional free time evolution (the buffer time) to the pulse such that the complete pulse duration T_d is 5 ns longer than T_p. The pulse parameters for the pulse we use to obtain the results in this Appendix are listed in Table VII. Note that we use single-qubit z-axis rotations $R_i^{(z)}(\phi_i)$ for every qubit to improve the gate performance.

Figures 13(a) and 13(b) show the diamond distance $\mu_\diamond$ [Fig. 13(a)] and the average infidelity $\mu_{\mathrm{IF_{avg}}}$ [Fig. 13(b)] as functions of the number of gates for the two-qubit NIGQC illustrated in Fig. 12. Here we executed a program which consists of 40 CZ gates in a row. In each panel we show the results for the two different cases: The adiabatic regime (blue solid line) and the nonadiabatic regime (green dash-dotted line).

As one can see, for the adiabatic case we find smaller gate errors and a smaller increase in gate errors over time.

TABLE VII. Control pulse parameters for the implementation of a $\mathrm{CZ}_{0,1}$ two-qubit gate on a two-qubit NIGQC as illustrated in Fig. 12. We use the parameters to specify the microwave pulse given by Eq. (C1). The first column shows the gate we implement, the second column shows the rise and fall time T_{RF} in nanoseconds, the third column shows the pulse duration without buffer time T_p in nanoseconds, the fourth column shows the pulse duration with buffer time T_d in nanoseconds, the fifth column shows the unitless pulse amplitude δ, and the sixth column shows the drive frequency $\omega^{(D)}$ in gigahertz. We use the effective Hamiltonian (7) to obtain the results.

Gate	T_{RF}	T_p	T_d	$\delta/2\pi$	$\omega^{(D)}/2\pi$
$\mathrm{CZ}_{0,1}$	24.674	299.406	304.406	0.082	0.808

Furthermore, after 40 CZ gate repetitions we find that the diamond distances deviate up to 0.8 and the average infidelities differ by about 0.6. Consequently, we find that neglecting the flux drive term in Eq. (10) leads to substantial deviations between the two NIGQC models.

Prototype gate-based quantum computers with similar device parameters are discussed in Refs. [46,48,49,54,65]. We find that most models which theoretically describe this device architecture model flux-tunable transmons adiabatically.

APPENDIX D: CONTROL PULSE PARAMETERS AND GATE-ERROR QUANTIFIERS

In this Appendix we provide the control pulse parameters listed in Tables VIII–XIX which we use to obtain the results in Sec. IV and the gate-error metrics listed in Tables XX–XXV we use to obtain Fig. 5.

The control pulse parameters for the circuit Hamiltonian (2) NIGQC model are listed in Tables VIII–XIII. Similarly, the control pulse parameters for the effective Hamiltonian (7) NIGQC model are listed in Tables XIV–XIX.

The gate-error metrics for the circuit Hamiltonian (2) NIGQC model are provided in Tables XX–XXII. Similarly, the gate-error metrics for the effective Hamiltonian (7) NIGQC model are listed in Tables XXIII–XXV.

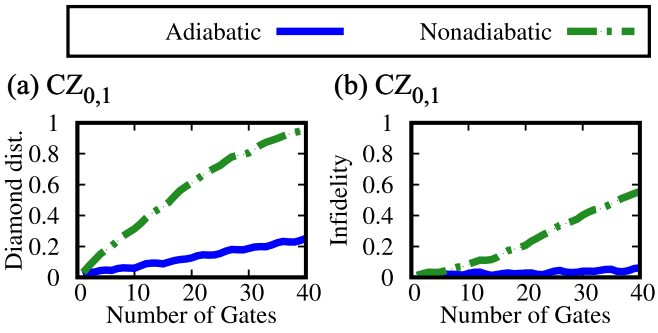

FIG. 13. Gate errors as functions of the number of gates for a program which executes 40 CZ gates in a row ($\mathrm{CZ}_{0,1}$) for (a) the diamond distance and (b) the average infidelity. We run the program on the two-qubit NIGQC illustrated in Fig. 12. The results are obtained with the effective Hamiltonian (2) and the device parameters listed in Table VI. We run the program two times on each NIGQC. On the first run, we model the flux-tunable transmons as adiabatic qubits. These results are displayed as a blue solid line. On the second run, we model the flux-tunable transmons as nonadiabatic qubits. These results are displayed as a green dash-dotted line. We can observe that the gate-error trajectories for the two cases can deviate up to 0.8 for the diamond distance and 0.6 for the average infidelity. Moreover, we can observe that the gate-error trajectories for both cases exhibit rather different qualitative behavior.

TABLE VIII. Control pulse parameters for the implementation of $R^{(x)}(\pi/2)$ rotations on a two-qubit NIGQC as illustrated in Fig. 1(a). We use the parameters to specify the microwave pulse given by Eq. (12). The first column shows the gate we implement, the second column shows the pulse duration T_d in nanoseconds, the third column shows the drive frequency $\omega^{(D)}$ in gigahertz, the fourth column shows the pulse amplitude a as a unitless quantity, the fifth column shows the envelope function parameter σ in nanoseconds, and the sixth column shows the DRAG amplitude b in nanoseconds. We use the circuit Hamiltonian (2) to obtain the results.

Gate	T_d	$\omega^{(D)}/2\pi$	a	σ	b
$R_0^{(x)}(\pi/2)$	52.250	4.196	0.004	12.082	0.072
$R_1^{(x)}(\pi/2)$	52.950	5.195	0.005	10.000	0.070

TABLE IX. Control pulse parameters for the implementation of CZ gates on a two-qubit NIGQC as illustrated in Fig. 1(a). We use the parameters to specify the unimodal pulse given by Eq. (13). The first column shows the gate we implement, the second column shows the pulse type, the third column shows the pulse time parameter T_p in nanoseconds, the fourth column shows the pulse duration T_d in nanoseconds, the fifth column shows the unitless pulse amplitude δ, and the sixth column shows the rise and fall parameter σ in nanoseconds. We use the circuit Hamiltonian (2) to obtain the results.

Gate	Pulse	T_p	T_d	$\delta/2\pi$	σ
$\mathrm{CZ}_{0,1}$	UMP	99.835	125.000	0.392	1.313

TABLE X. Control pulse parameters for the implementation of $R^{(x)}(\pi/2)$ rotations on a three-qubit NIGQC as illustrated in Fig. 1(b). The units are the same as in Table VIII. We use the circuit Hamiltonian (2) to obtain the results.

Gate	T_d	$\omega^{(D)}/2\pi$	a	σ	b
$R_0^{(x)}(\pi/2)$	52.250	4.196	0.004	12.093	0.168
$R_1^{(x)}(\pi/2)$	52.950	5.190	0.004	9.997	0.067
$R_2^{(x)}(\pi/2)$	52.950	5.695	0.004	10.011	0.066

TABLE XI. Control pulse parameters for the implementation of CZ gates on a three-qubit NIGQC as illustrated in Fig. 1(b). The units are the same as in Table IX. We use the effective Hamiltonian (2) to obtain the results.

Gate	Pulse	T_p	T_d	$\delta/2\pi$	σ
$\mathrm{CZ}_{0,1}$	UMP	96.026	125.000	0.391	1.823
$\mathrm{CZ}_{1,2}$	UMP	75.367	110.000	0.276	0.513

TABLE XII. Control pulse parameters for the implementation of $R^{(x)}(\pi/2)$ rotations on a four-qubit NIGQC as illustrated in Fig. 1(c). The units are the same as in Table VIII. We use the circuit Hamiltonian (2) to obtain the results.

Gate	T_d	$\omega^{(D)}/2\pi$	a	σ	b
$R_0^{(x)}(\pi/2)$	52.250	4.193	0.004	12.378	0.047
$R_1^{(x)}(\pi/2)$	52.950	5.190	0.004	10.255	0.063
$R_2^{(x)}(\pi/2)$	52.950	5.689	0.004	10.312	0.065
$R_3^{(x)}(\pi/2)$	52.950	4.951	0.005	10.191	0.012

TABLE XIII. Control pulse parameters for the implementation of CZ gates on a four-qubit NIGQC as illustrated in Fig. 1(c). The units are the same as in Table IX. We use the circuit Hamiltonian (2) to obtain the results.

Gate	Pulse	T_p	T_d	$\delta/2\pi$	σ
$CZ_{0,1}$	UMP	100.241	125.000	0.392	1.283
$CZ_{1,2}$	UMP	68.046	90.000	0.275	0.182
$CZ_{2,3}$	UMP	80.500	94.000	0.320	0.500
$CZ_{0,3}$	UMP	97.708	116.000	0.353	1.458

TABLE XIV. Control pulse parameters for the implementation of $R^{(x)}(\pi/2)$ rotations on a two-qubit NIGQC as illustrated in Fig. 1(a). We use the parameters to specify the microwave pulse given by Eq. (12). The first column shows the gate we implement, the second column shows the pulse duration T_d in nanoseconds, the third column shows the drive frequency $\omega^{(D)}$ in gigahertz, the fourth column shows the pulse amplitude a as a unitless quantity, the fifth column shows the envelope function parameter σ in nanoseconds, and the sixth column shows the DRAG amplitude b in nanoseconds. We use the effective Hamiltonian (7) to obtain the results.

Gate	T_d	$\omega^{(D)}/2\pi$	a	σ	b
$R_0^{(x)}(\pi/2)$	52.250	4.196	0.058	12.082	0.072
$R_1^{(x)}(\pi/2)$	52.950	5.195	0.065	10.000	0.070

TABLE XV. Control pulse parameters for the implementation of CZ gates on a two-qubit NIGQC as illustrated in Fig. 1(a). We use the parameters to specify the unimodal pulse and bimodal pulse given by Eqs. (13) and (14), respectively. The first column shows the gate we implement, the second column shows the pulse type, the third column shows the pulse time parameter T_p in nanoseconds, the fourth column shows the pulse duration T_d in nanoseconds, the fifth column shows the unitless pulse amplitude δ, and the sixth column shows the rise and fall parameter σ in nanoseconds. We use the effective Hamiltonian (7) to obtain the results.

Gate	Pulse	T_p	T_d	$\delta/2\pi$	σ
$CZ_{0,1}$	UMP	87.258	95.000	0.391	0.459
$CZ_{0,1}$	BMP	88.570	95.000	0.392	0.394

TABLE XVI. Control pulse parameters for the implementation of $R^{(x)}(\pi/2)$ rotations on a three-qubit NIGQC as illustrated in Fig. 1(b). The units are the same as in Table XIV. We use the effective Hamiltonian (7) to obtain the results.

Gate	T_d	$\omega^{(D)}/2\pi$	a	σ	b
$R_0^{(x)}(\pi/2)$	52.250	4.196	0.058	12.082	0.072
$R_1^{(x)}(\pi/2)$	52.950	5.189	0.065	10.000	0.070
$R_2^{(x)}(\pi/2)$	52.950	5.694	0.066	9.990	0.032

TABLE XVII. Control pulse parameters for the implementation of CZ gates on a three-qubit NIGQC as illustrated in Fig. 1(b). The units are the same as in Table XV. We use the effective Hamiltonian (7) to obtain the results.

Gate	Pulse	T_p	T_d	$\delta/2\pi$	σ
$CZ_{0,1}$	UMP	87.252	95.006	0.391	0.494
$CZ_{0,1}$	BMP	90.057	92.188	0.391	0.420
$CZ_{1,2}$	UMP	68.831	80.000	0.276	0.554

TABLE XVIII. Control pulse parameters for the implementation of $R^{(x)}(\pi/2)$ rotations on a four-qubit NIGQC as illustrated in Fig. 1(c). The units are the same as in Table XIV. We use the effective Hamiltonian (7) to obtain the results.

Gate	T_d	$\omega^{(D)}/2\pi$	a	σ	b
$R_0^{(x)}(\pi/2)$	52.250	4.191	0.058	12.082	0.072
$R_1^{(x)}(\pi/2)$	52.950	5.189	0.065	10.000	0.070
$R_2^{(x)}(\pi/2)$	52.950	5.688	0.066	9.990	0.032
$R_3^{(x)}(\pi/2)$	52.950	4.950	0.066	9.990	0.032

TABLE XIX. Control pulse parameters for the implementation of CZ gates on a four-qubit NIGQC as illustrated in Fig. 1(c). The units are the same as in Table XV. We use the effective Hamiltonian (7) to obtain the results.

Gate	Pulse	T_p	T_d	$\delta/2\pi$	σ
$CZ_{0,1}$	UMP	87.254	95.013	0.391	0.453
$CZ_{0,1}$	BMP	89.925	98.114	0.392	0.400
$CZ_{1,2}$	UMP	67.802	115.238	0.275	0.338
$CZ_{2,3}$	UMP	71.620	98.197	0.320	0.543
$CZ_{0,3}$	UMP	92.616	124.768	0.353	1.877

TABLE XX. Gate-error quantifiers for $R^{(x)}(\pi/2)$ rotations and CZ gates for a two-qubit NIGQC as illustrated in Fig. 1(a). The gate-error quantifiers are obtained with the circuit Hamiltonian (2), the device parameters listed in Table I, and the pulse parameters listed in Tables VIII and IX. The first column shows the target gate, the second column shows the pulse type [see Figs. 2(a)–2(c)], the third column shows the diamond distance $\mu_\diamond$ given by Eqs. (28) and (29), the fourth column shows the average infidelity $\mu_{\mathrm{IF}_{\mathrm{avg}}}$ given by Eq. (24), and the fifth column shows the leakage measure μ_{leak} given by Eq. (26).

Gate	Pulse	$\mu_\diamond$	$\mu_{\mathrm{IF}_{\mathrm{avg}}}$	μ_{leak}
$R_0^{(x)}(\pi/2)$	MP	0.0093	0.0004	0.0004
$R_1^{(x)}(\pi/2)$	MP	0.0080	0.0004	0.0004
$\mathrm{CZ}_{0,1}$	UMP	0.0290	0.0011	0.0008

TABLE XXI. Gate-error quantifiers for $R^{(x)}(\pi/2)$ rotations and CZ gates for a three-qubit NIGQC as illustrated in Fig. 1(b). The gate-error quantifiers are obtained with the circuit Hamiltonian (2), the device parameters listed in Table I, and the pulse parameters listed in Tables X and XI. The rows and columns show the same unitless quantities as in Table XX.

Gate	Pulse	$\mu_\diamond$	$\mu_{\mathrm{IF}_{\mathrm{avg}}}$	μ_{leak}
$R_0^{(x)}(\pi/2)$	MP	0.044	0.003	0.002
$R_1^{(x)}(\pi/2)$	MP	0.038	0.002	0.001
$R_2^{(x)}(\pi/2)$	MP	0.039	0.002	0.001
$\mathrm{CZ}_{0,1}$	UMP	0.044	0.010	0.010
$\mathrm{CZ}_{1,2}$	UMP	0.012	0.002	0.002

TABLE XXII. Gate-error quantifiers for $R^{(x)}(\pi/2)$ rotations and CZ gates for a four-qubit NIGQC as illustrated in Fig. 1(c). The gate-error quantifiers are obtained with the circuit Hamiltonian (2), the device parameters listed in Table I, and the pulse parameters listed in Tables XII and XIII. The rows and columns show the same unitless quantities as in Table XX.

Gate	Pulse	$\mu_\diamond$	$\mu_{\mathrm{IF}_{\mathrm{avg}}}$	μ_{leak}
$R_0^{(x)}(\pi/2)$	MP	0.058	0.004	0.002
$R_1^{(x)}(\pi/2)$	MP	0.054	0.003	0.002
$R_2^{(x)}(\pi/2)$	MP	0.053	0.003	0.002
$R_3^{(x)}(\pi/2)$	MP	0.057	0.004	0.002
$\mathrm{CZ}_{0,1}$	UMP	0.031	0.005	0.004
$\mathrm{CZ}_{1,2}$	UMP	0.144	0.029	0.018
$\mathrm{CZ}_{2,3}$	UMP	0.073	0.008	0.005
$\mathrm{CZ}_{0,3}$	UMP	0.046	0.005	0.003

TABLE XXIII. Gate-error quantifiers for $R^{(x)}(\pi/2)$ rotations and CZ gates for a two-qubit NIGQC as illustrated in Fig. 1(a). The gate-error quantifiers are obtained with the effective Hamiltonian (7), the device parameters listed in Table I, and the pulse parameters listed in Tables XIV and XV. The first column shows the target gate, the second column shows the pulse type [see Figs. 2(a)–2(c)], the third column shows the diamond distance $\mu_\diamond$ given by Eqs. (28) and (29), the fourth column shows the average infidelity $\mu_{\mathrm{IF}_{\mathrm{avg}}}$ given by Eq. (24), and the fifth column shows the leakage measure μ_{leak} given by Eq. (26).

Gate	Pulse	$\mu_\diamond$	$\mu_{\mathrm{IF}_{\mathrm{avg}}}$	μ_{leak}
$R_0^{(x)}(\pi/2)$	MP	0.0089	0.0004	0.0004
$R_1^{(x)}(\pi/2)$	MP	0.0090	0.0004	0.0004
$\mathrm{CZ}_{0,1}$	UMP	0.0424	0.0012	0.0005
$\mathrm{CZ}_{0,1}$	BMP	0.0167	0.0006	0.0005

TABLE XXIV. Gate-error quantifiers for $R^{(x)}(\pi/2)$ rotations and CZ gates for a three-qubit NIGQC as illustrated in Fig. 1(b). The gate-error quantifiers are obtained with the effective Hamiltonian (7), the device parameters listed in Table I, and the pulse parameters listed in Tables XVI and XVII. The rows and columns show the same unitless quantities as in Table XXIII.

Gate	Pulse	$\mu_\diamond$	$\mu_{\mathrm{IF}_{\mathrm{avg}}}$	μ_{leak}
$R_0^{(x)}(\pi/2)$	MP	0.046	0.003	0.002
$R_1^{(x)}(\pi/2)$	MP	0.040	0.002	0.002
$R_2^{(x)}(\pi/2)$	MP	0.039	0.002	0.002
$\mathrm{CZ}_{0,1}$	UMP	0.057	0.003	0.002
$\mathrm{CZ}_{0,1}$	BMP	0.031	0.004	0.004
$\mathrm{CZ}_{1,2}$	UMP	0.028	0.006	0.006

TABLE XXV. Gate-error quantifiers for $R^{(x)}(\pi/2)$ rotations and CZ gates for a four-qubit NIGQC as illustrated in Fig. 1(c). The gate-error quantifiers are obtained with the effective Hamiltonian (7), the device parameters listed in Table I, and the pulse parameters listed in Tables XVIII and XIX. The rows and columns show the same unitless quantities as in Table XXIII.

Gate	Pulse	$\mu_\diamond$	$\mu_{\mathrm{IF}_{\mathrm{avg}}}$	μ_{leak}
$R_0^{(x)}(\pi/2)$	MP	0.060	0.004	0.003
$R_1^{(x)}(\pi/2)$	MP	0.056	0.003	0.002
$R_2^{(x)}(\pi/2)$	MP	0.054	0.003	0.002
$R_3^{(x)}(\pi/2)$	MP	0.060	0.004	0.002
$\mathrm{CZ}_{0,1}$	UMP	0.051	0.004	0.003
$\mathrm{CZ}_{0,1}$	BMP	0.041	0.004	0.004
$\mathrm{CZ}_{1,2}$	UMP	0.146	0.015	0.005
$\mathrm{CZ}_{2,3}$	UMP	0.078	0.010	0.007
$\mathrm{CZ}_{0,3}$	UMP	0.058	0.005	0.003

[1] M. A. Nielsen and I. L. Chuang, *Quantum Computation and Quantum Information*, 10th ed. (Cambridge University Press, Cambridge, 2011).

[2] J. Watrous, *The Theory of Quantum Information* (Cambridge University Press, Cambridge, 2018).

[3] D. Willsch, M. Nocon, F. Jin, H. DeRaedt, and K. Michielsen, Phys. Rev. A **96**, 062302 (2017).

[4] K. Michielsen, M. Nocon, D. Willsch, F. Jin, T. Lippert, and H. De Raedt, Comput. Phys. Commun. **220**, 44 (2017).

[5] M. A. Nielsen, Phys. Lett. A **303**, 249 (2002).

[6] F. Jin, D. Willsch, M. Willsch, H. Lagemann, K. Michielsen, and H. De Raedt, J. Phys. Soc. Jpn. **90**, 012001 (2021).

[7] A. Y. Kitaev, Russ. Math. Surv. **52**, 1191 (1997).

[8] Y. R. Sanders, J. J. Wallman, and B. C. Sanders, New J. Phys. **18**, 012002 (2015).

[9] M. A. Rol, F. Battistel, F. K. Malinowski, C. C. Bultink, B. M. Tarasinski, R. Vollmer, N. Haider, N. Muthusubramanian, A. Bruno, B. M. Terhal, and L. DiCarlo, Phys. Rev. Lett. **123**, 120502 (2019).

[10] M. Werninghaus, D. J. Egger, F. Roy, S. Machnes, F. K. Wilhelm, and S. Filipp, npj Quantum Inf. **7**, 14 (2021).

[11] S. Krinner, S. Storz, P. Kurpiers, P. Magnard, J. Heinsoo, R. Keller, J. Lütolf, C. Eichler, and A. Wallraff, EPJ Quantum Technol. **6**, 2 (2019).

[12] J. J. Burnett, A. Bengtsson, M. Scigliuzzo, D. Niepce, M. Kudra, P. Delsing, and J. Bylander, npj Quantum Inf. **5**, 54 (2019).

[13] M. McEwen, L. Faoro, K. Arya, A. Dunsworth, T. Huang, S. Kim, B. Burkett, A. Fowler, F. Arute, J. C. Bardin, A. Bengtsson, A. Bilmes, B. B. Buckley, N. Bushnell, Z. Chen, R. Collins, S. Demura, A. R. Derk, C. Erickson, M. Giustina *et al.*, Nat. Phys. **18**, 107 (2022).

[14] N. Lacroix, C. Hellings, C. K. Andersen, A. Di Paolo, A. Remm, S. Lazar, S. Krinner, G. J. Norris, M. Gabureac, J. Heinsoo, A. Blais, C. Eichler, and A. Wallraff, PRX Quantum **1**, 020304 (2020).

[15] S. Krinner, S. Lazar, A. Remm, C. K. Andersen, N. Lacroix, G. J. Norris, C. Hellings, M. Gabureac, C. Eichler, and A. Wallraff, Phys. Rev. Appl. **14**, 024042 (2020).

[16] C. K. Andersen, A. Remm, S. Lazar, S. Krinner, N. Lacroix, G. J. Norris, M. Gabureac, C. Eichler, and A. Wallraff, Nat. Phys. **16**, 875 (2020).

[17] C. A. Balanis, *Advanced Engineering Electromagnetics* (Wiley, New York, 2012), Sec. 1.4.

[18] H. Lagemann, D. Willsch, M. Willsch, F. Jin, H. De Raedt, and K. Michielsen, Phys. Rev. A **106**, 022615 (2022).

[19] H. DeRaedt, Comput. Phys. Rep. **7**, 1 (1987).

[20] J. Huyghebaert and H. De Raedt, J. Phys. A: Math. Gen. **23**, 5777 (1990).

[21] D. Vion, A. Aassime, A. Cottet, P. Joyez, H. Pothier, C. Urbina, D. Esteve, and M. H. Devoret, Science **296**, 886 (2002).

[22] J. Koch, T. M. Yu, J. Gambetta, A. A. Houck, D. I. Schuster, J. Majer, A. Blais, M. H. Devoret, S. M. Girvin, and R. J. Schoelkopf, Phys. Rev. A **76**, 042319 (2007).

[23] X. You, J. A. Sauls, and J. Koch, Phys. Rev. B **99**, 174512 (2019).

[24] R.-P. Riwar and D. P. DiVincenzo, npj Quantum Inf. **8**, 36 (2022).

[25] N. Didier, E. A. Sete, M. P. da Silva, and C. Rigetti, Phys. Rev. A **97**, 022330 (2018).

[26] F. Motzoi, J. M. Gambetta, P. Rebentrost, and F. K. Wilhelm, Phys. Rev. Lett. **103**, 110501 (2009).

[27] D. C. McKay, C. J. Wood, S. Sheldon, J. M. Chow, and J. M. Gambetta, Phys. Rev. A **96**, 022330 (2017).

[28] A. Blais, A. L. Grimsmo, S. M. Girvin, and A. Wallraff, Rev. Mod. Phys. **93**, 025005 (2021); see in particular Sec. VII B 2.

[29] D. Willsch, Supercomputer simulations of transmon quantum computers, Ph.D. thesis, RWTH Aachen University, 2020, https://juser.fz-juelich.de/record/885927.

[30] N. Johnston, D. Kribs, and V. Paulsen, Quantum Inf. Comput. **9**, 16 (2009).

[31] D. Krause, J. Large Scale Res. Fac. **5**, A135 (2019).

[32] L. DiCarlo, J. M. Chow, J. M. Gambetta, L. S. Bishop, B. R. Johnson, D. I. Schuster, J. Majer, A. Blais, L. Frunzio, S. M. Girvin, and R. J. Schoelkopf, Nature (London) **460**, 240 (2009).

[33] L. DiCarlo, M. D. Reed, L. Sun, B. R. Johnson, J. M. Chow, J. M. Gambetta, L. Frunzio, S. M. Girvin, M. H. Devoret, and R. J. Schoelkopf, Nature (London) **467**, 574 (2010).

[34] S. Weinberg, *Lectures on Quantum Mechanics*, 2nd ed. (Cambridge University Press, Cambridge, 2015).

[35] F. Hund, Z. Phys. **40**, 742 (1927).

[36] J. von Neumann and E. P. Wigner, in *The Collected Works of Eugene Paul Wigner. Part A: The Scientific Papers*, edited by A. S. Wightman (Springer, Berlin, 1993), pp. 291–293.

[37] F. Uhlig, arXiv:2002.01274.

[38] U. Srinivasan and R. Kidambi, arXiv:2006.14254.

[39] Intel® oneAPI Math Kernel Library, https://www.intel.com/content/www/us/en/developer/tools/oneapi/onemkl.html#gs.axn2um (Intel Corporation, Santa Clara).

[40] S. Krinner, N. Lacroix, A. Remm, A. Di Paolo, E. Genois, C. Leroux, C. Hellings, S. Lazar, F. Swiadek, J. Herrmann, G. J. Norris, C. K. Andersen, M. Müller, A. Blais, C. Eichler, and A. Wallraff, Nature (London) **605**, 669 (2022).

[41] F. Arute, K. Arya, R. Babbush, D. Bacon, J. Bardin, R. Barends, R. Biswas, S. Boixo, F. Brandao, D. Buell, B. Burkett, Y. Chen, J. Chen, B. Chiaro, R. Collins, W. Courtney, A. Dunsworth, E. Farhi, B. Foxen, A. Fowler *et al.*, Nature (London) **574**, 505 (2019); see in particular Sec. VI C 1 of the Supplemental Material.

[42] A. J. Baker, G. B. P. Huber, N. J. Glaser, F. Roy, I. Tsitsilin, S. Filipp, and M. J. Hartmann, Appl. Phys. Lett. **120**, 054002 (2022).

[43] J. Cohen, A. Petrescu, R. Shillito, and A. Blais, PRX Quantum **4**, 020312 (2023).

[44] J. B. Hertzberg, E. J. Zhang, S. Rosenblatt, E. Magesan, J. A. Smolin, J.-B. Yau, V. P. Adiga, M. Sandberg, M. Brink, J. M. Chow, and J. S. Orcutt, npj Quantum Inf. **7**, 129 (2021).

[45] S. G. Johnson, The NLopt nonlinear-optimization package, http://github.com/stevengj/nlopt.

[46] X. Gu, J. Fernández-Pendás, P. Vikstål, T. Abad, C. Warren, A. Bengtsson, G. Tancredi, V. Shumeiko, J. Bylander, G. Johansson, and A. F. Kockum, PRX Quantum **2**, 040348 (2021).

[47] N. Wittler, F. Roy, K. Pack, M. Werninghaus, A. S. Roy, D. J. Egger, S. Filipp, F. K. Wilhelm, and S. Machnes, Phys. Rev. Appl. **15**, 034080 (2021).

[48] D. C. McKay, S. Filipp, A. Mezzacapo, E. Magesan, J. M. Chow, and J. M. Gambetta, Phys. Rev. Appl. **6**, 064007 (2016).

[49] M. Roth, M. Ganzhorn, N. Moll, S. Filipp, G. Salis, and S. Schmidt, Phys. Rev. A **96**, 062323 (2017).
[50] F. Yan, P. Krantz, Y. Sung, M. Kjaergaard, D. L. Campbell, T. P. Orlando, S. Gustavsson, and W. D. Oliver, Phys. Rev. Appl. **10**, 054062 (2018).
[51] D. Willsch, D. Rieger, P. Winkel, M. Willsch, C. Dickel, J. Krause, Y. Ando, R. Lescanne, Z. Leghtas, N. T. Bronn, P. Deb, O. Lanes, Z. K. Minev, B. Dennig, S. Geisert, S. Günzler, S. Ihssen, P. Paluch, T. Reisinger, R. Hanna *et al.*, arXiv:2302.09192.
[52] T. Roth, R. Ma, and W. C. Chew, IEEE Antenn. Propag. Mag. **65**, 8 (2023).
[53] B. Foxen, C. Neill, A. Dunsworth, P. Roushan, B. Chiaro, A. Megrant, J. Kelly, Z. Chen, K. Satzinger, R. Barends, F. Arute, K. Arya, R. Babbush, D. Bacon, J. C. Bardin, S. Boixo, D. Buell, B. Burkett, Y. Chen, R. Collins *et al.* (Google AI Quantum), Phys. Rev. Lett. **125**, 120504 (2020).
[54] M. Ganzhorn, G. Salis, D. J. Egger, A. Fuhrer, M. Mergenthaler, C. Müller, P. Müller, S. Paredes, M. Pechal, M. Werninghaus, and S. Filipp, Phys. Rev. Res. **2**, 033447 (2020).
[55] R. Alicki, M. Horodecki, P. Horodecki, and R. Horodecki, Phys. Rev. A **65**, 062101 (2002).
[56] R. Alicki, D. A. Lidar, and P. Zanardi, Phys. Rev. A **73**, 052311 (2006).
[57] B. M. Terhal and G. Burkard, Phys. Rev. A **71**, 012336 (2005).
[58] H. A. Lagemann, Real-time simulations of transmon systems with time-dependent Hamiltonian models, Ph.D. thesis, RWTH Aachen University, 2023; see in particular Secs. 4.1–4.8, https://publications.rwth-aachen.de/record/953773.
[59] H. Lagemann, Development and implementation of a gate-based quantum computer simulator for high-dimensional Hilbert spaces, Master's thesis, RWTH Aachen University, 2019, https://juser.fz-juelich.de/record/868377.
[60] C. E. Murray, Mater. Sci. Eng. R **146**, 100646 (2021).
[61] J. M. Martinis and A. Megrant, arXiv:1410.5793.
[62] E. Farhi, J. Goldstone, and S. Gutmann, arXiv:1411.4028.
[63] D. Willsch, M. Willsch, F. Jin, K. Michielsen, and H. De Raedt, Comput. Phys. Commun. **278**, 108411 (2022).
[64] W. Fenchel, Can. J. Math. **1**, 73 (1949).
[65] A. Bengtsson, P. Vikstål, C. Warren, M. Svensson, X. Gu, A. F. Kockum, P. Krantz, C. Križan, D. Shiri, I.-M. Svensson, G. Tancredi, G. Johansson, P. Delsing, G. Ferrini, and J. Bylander, Phys. Rev. Appl. **14**, 034010 (2020).